

**HIGH-RESOLUTION TOPOMAPPING
OF CANDIDATE MER LANDING SITES
WITH MARS ORBITER CAMERA NARROW-ANGLE IMAGES**

Randolph L. Kirk, Elpitha Howington-Kraus, Bonnie Redding, Donna Galuszka, Trent M. Hare,
Brent A. Archinal, Laurence A. Soderblom, and Janet M. Barrett

Astrogeology Team
U.S. Geological Survey
2255 N. Gemini Dr.
Flagstaff, Arizona, 86004 USA
Tel.: 928-556-7020
Fax: 928-556-7014
rkirk@usgs.gov

Submitted to
MER Special Issue of Journal of Geophysical Research, Planets
6 June 2003

Revised
14 August 2003

Index Terms: 1224, 5464, 5494, 5470, 6225

Keywords: Mars, Mars Exploration Rovers, Landing Sites, Topography, Photogrammetry,
Photoclinometry

ABSTRACT

We analyzed narrow-angle Mars Orbiter Camera (MOC-NA) images to produce high-resolution digital elevation models (DEMs) in order to provide topographic and slope information needed to assess the safety of candidate landing sites for the Mars Exploration Rovers (MER) and to assess the accuracy of our results by a variety of tests. The mapping techniques developed also support geoscientific studies and can be used with all present and planned Mars-orbiting scanner cameras. Photogrammetric analysis of MOC stereopairs yields DEMs with 3-pixel (typically 10 m) horizontal resolution, vertical precision consistent with ~ 0.22 pixel matching errors (typically a few meters), and slope errors of $1\text{--}3^\circ$. These DEMs are controlled to the MOLA global dataset and consistent with it at the limits of resolution. Photoclinometry yields DEMs with single-pixel (typically ~ 3 m) horizontal resolution and sub-meter vertical precision. Where the surface albedo is uniform the dominant error is 10–20% relative uncertainty in the amplitude of topography and slopes after "calibrating" photoclinometry against a stereo DEM to account for the influence of atmospheric haze. We mapped portions of seven candidate MER sites and the Mars Pathfinder site. Safety of the final four sites (Elysium, Gusev, Isidis, and Meridiani) was assessed by mission engineers by simulating landings on our DEMs of "hazard units" mapped in the sites, with results weighted by the probability of landing on those units; summary slope statistics show that most hazard units are smooth, with only small areas of etched terrain in Gusev crater posing a slope hazard.

1. Introduction

Accurate topographic information, and, in particular, high-resolution digital elevation models are of intense interest for all phases of Mars exploration and scientific investigation, from

landing site selection to the quantitative analysis of the morphologic record of surface processes. The need to select geologically interesting yet safe landing sites for the two Mars Exploration Rovers that will arrive in January 2004 created an especially urgent need for topographic and slope information about candidate sites [Golombek *et al.*, 2003, this issue]. The MER landing system is similar to that used for Mars Pathfinder and incorporates a cluster of airbags to protect the spacecraft on impact. Surface slopes on a variety of lengthscales can pose a hazard to this system. For example, even modest slopes ($\geq 2^\circ$) over kilometer baselines may cause the spacecraft to roll at high speed and thus be damaged, and intermediate slopes ($\geq 5^\circ$) over hundred-meter baselines could cause the final stages of landing (parachute jettison and retrorocket fire) to occur at an unsafe altitude. Finally, slopes at the scale of the airbag cluster (~ 5 m diameter) could cause the spacecraft to bounce either too vertically (leading to "stroking out" and structural damage on the next bounce) or too horizontally (tearing the airbags on the following impact). As a rough estimate, slopes $\geq 15^\circ$ at the airbag scale are considered dangerous, though the potential for damage depends on the rocks present at the site and on random details of the trajectory and must thus be assessed by detailed simulations.

Unfortunately, though MOLA altimetry can be used to assess the slope hazards over kilometer and even 100-m baselines, the availability of extremely high resolution topographic data needed to determine slopes at the airbag scale has hitherto been limited. The current "gold standard" for martian topographic data, MOLA [Zuber *et al.*, 1992; Smith *et al.*, 1999; 2001] has collected data globally with astonishingly high accuracy, but the sample spacing of this dataset is only about 300 m along track and, in many places near the equator, adjacent MOLA ground tracks are separated by gaps of one to several kilometers. The MOLA pulsewidth also provides information about relief over smaller distances, but only as an average over the ~ 160 m footprint

of the laser pulse [Garvin *et al.*, 1999, Haldemann and Anderson, 2002]. Viking Orbiter images provide stereo coverage of the entire planet at low resolution and expected vertical precision (EP, a function of image resolution and stereo viewing geometry as discussed below) but highest resolution stereo coverage only of extremely limited areas [Kirk *et al.*, 1999b]. Given that the minimum separation of independent stereo measurements is about 3 pixels because of the necessity of matching finite-sized image patches, the highest resolution Viking images, at about 8 m/pixel, support stereomapping only at horizontal resolutions >24 m. Two-dimensional photoclinometry, or shape-from-shading [Kirk, 1987; Kirk *et al.*, 2003a], can be used to produce DEMs at the pixel resolution from single images. Since single-image coverage is much more abundant than stereo coverage, this in principle increases the likelihood that a given region can be mapped as well as improving the DEM resolution. Photoclinometry must be calibrated against topographic data from another source if quantitatively accurate results are to be obtained, however, so in practice stereo coverage is still needed. In any case, the best (nonstereo) Viking images of the candidate MER landing sites have resolutions much too poor to be useful.

The MOC-NA camera, with a maximum resolution of 1.5 m/pixel [Malin *et al.*, 1992; 1998; Malin and Edgett, 2001], offers the prospect of stereotopographic mapping at a horizontal resolution of ~ 5 m and EP ~ 1 m, though the majority of images used in this study were obtained at ≥ 3 m/pixel and have correspondingly poorer stereo resolution and EP. MOC-NA stereo coverage is limited because, until late in the prime mission, most images were obtained with nadir pointing and were not targeted to overlap one another. More than 150 MOC-MOC stereopairs were nonetheless obtained by mission phase E14 [Caplinger, 2003]. It is also likely that some MOC images will provide useful stereo coverage when paired with oblique Viking Orbiter images or, eventually, with THEMIS visible-band images. In addition, obtaining images,

including stereopairs, of candidate MER landing sites has been an important objective of the MGS extended mission, and these images have been made available for site assessment prior to their formal release. For all these reasons, a capability for stereomapping with the MOC-NA images is highly desirable and has been developed independently by our group [Kirk *et al.*, 2001a; 2002a; 2002b; 2003b] and by others [Ivanov and Lorre, 2002; Ivanov, 2003; Caplinger, 2003]. The pushbroom scanner geometry of the camera means that stereo software used for framing cameras (e.g., those of Viking Orbiter) must be modified in order to be used with MOC. The other main challenges in working with MOC data are identifying suitable stereopairs and providing adequate geodetic control for such high-resolution images.

Photoclinometric software initially developed for framing cameras [Kirk, 1987; Kirk *et al.*, 2003a] required only minor modifications for use with MOC images, but the results depend on the accuracy of atmospheric and surface radiative transfer models, and in particular on accurate calibration of the atmospheric haze contribution to each image. Our photoclinometric mapping of landing sites relies heavily on high-resolution stereo data for this calibration but improves the horizontal resolution to the single-pixel level.

In this paper we describe our methods for deriving stereo and calibrated photoclinometric DEMs from MOC-NA images, assess the accuracy of our methods with a variety of tests involving real and simulated data, and describe our results for the topographic slopes in the Mars Pathfinder and seven candidate MER landing sites.

2. Methodology

2.1 Stereomapping Software Implementation

The software packages, specialized hardware, and workflow for the MOC mapping reported here are the same as those we use for stereoanalysis of a wide range of planetary datasets [*Kirk et al.*, 1999a; 2000a; *Rosiek et al.*, 2001a; 2001b; *Howington-Kraus et al.*, 2002a; 2002b]. We use the USGS in-house digital cartographic software ISIS [*Eliason*, 1997; *Gaddis et al.*, 1997; *Torson and Becker*, 1997] for mission-specific data ingestion and calibration steps, as well as "two-dimensional" processing such as map-projection and image mosaicking. Our commercial digital photogrammetric workstation, an LH Systems DPW-790 running SOCET SET software (© BAE Systems) [*Miller and Walker*, 1993; 1995] includes special hardware for stereo display of images and graphics, and is used mainly for such "three-dimensional" processing steps as automatic and manual measurement of image tiepoints; bundle-block adjustment of image orientations to conform to geodetic control; and automatic extraction and manual editing of DEMs. The ability to view DEM data as graphics overlaid on the images in stereo in order to detect and interactively edit errors is the single most important reason for using the commercial system.

In order to work with planetary data, we have written a set of translator programs drawing on both ISIS and the SOCET SET Developer's Toolkit (DEVKIT) to import images and geometric metadata from ISIS into SOCET SET and export DEMs and orthoimage maps back to ISIS. Images from planetary framing cameras (e.g., Viking, Clementine) can then be analyzed with the framing camera sensor model software supplied as a basic part of SOCET SET. (A sensor model consists of software that carries out the transformation between image and ground coordinates and vice versa, plus a variety of housekeeping routines.) The DEVKIT lets us implement and install sensor models for other instruments, such as the Magellan synthetic aperture radar [*Howington-Kraus et al.*, 2002a]. After beginning a similar in-house development of a sensor

model for the MOC camera, we were able to take a substantial "shortcut" by making use of the generic pushbroom scanner model included in SOCET SET and writing only the software needed to import MOC images and set them up for use with this model.

The generic scanner model computes a physically realistic description of the process by which a scanner image is built up. It is "generic" in the sense that the following parameters must be specified and can be different for different cameras and/or images from the same camera:

- Image size; relation between line number and time
- Camera focal length and lens distortion polynomial
- Camera trajectory in the form of position and velocity at a series of equally spaced times spanning acquisition of the image, to be interpolated
- Camera orientation relative to the vertical and flight direction (nominally assumed constant)
- Corrections to the trajectory and orientation, normally initialized as zero and estimated as part of the bundle-adjustment process
 - Position and velocity offsets in the along-track, across-track, and vertical directions
 - Angular offsets around three orthogonal axes, angular velocities, and angular accelerations

These parameters suffice to describe not only the MOC-NA but also the wide-angle (WA) cameras, which have been used to obtain global stereo coverage with 240-m resolution [Caplinger and Malin, 2001] (the optical distortion of the WA cameras is too strong to be modeled accurately by SOCET SET, so that it is necessary to resample the images to correct this distortion before stereo processing); the infrared scanner of the THEMIS instrument on the Mars Odyssey Orbiter [Christensen *et al.*, 1999]; the Mars Express High Resolution Stereo Camera (HRSC) with multiple detector lines for single-pass stereo imaging at 10 m/pixel [Albertz *et al.*,

1992]; and the HiRISE scanner for the 2005 Mars Reconnaissance Orbiter mission [McEwen *et al.*, 2002]. Not only can the generic scanner model be used with images from any of these cameras, SOCET SET permits bundle-adjustment and stereo DEM collection with any combination of scanner and framing camera data in a single project. To date, we have written software to collect the necessary information from both MOC-NA and WA image labels, convert geometric quantities from the inertial coordinate system used by ISIS to the local Cartesian system used by SOCET SET, and write this supporting data in the needed format. The techniques we then use will be applicable to the other datasets once these datasets and the software to ingest them are available.

A significant limitation of the software that affects its use with MOC-NA images is the nominally constant orientation of the camera. Images obtained (during the aerobraking phase of the MGS mission) by rotating the spacecraft do not fit this model, and our attempts to represent the spacecraft rotation by using the adjustable parameters were unsuccessful. An enhancement of the sensor model in the most recent release allows an arbitrary time history of camera orientation to be specified but we have yet to test this feature. The limited set of adjustable parameters in the model also has its drawbacks, and this is unlikely to be changed. The low-order (smooth) position and pointing corrections possible with these parameters cannot address the high-frequency undulations of the MGS spacecraft that plague some MOC stereopairs as discussed below. Nor does the SOCET SET bundle-adjustment software understand that images from a multiline scanner such as HRSC come from the same spacecraft and are subject to the same position and pointing corrections as a function of time. We are currently implementing more capable bundle-adjustment software outside SOCET SET in order to address these shortcomings

2.2. Identification of Stereoimagery

Identifying suitable pairs of MOC-NA images for stereoanalysis is a significant challenge, given that more than 50,000 images have been released to date but a typical image covers only about one one-millionth of Mars's surface area. We have pursued several approaches to identifying pairs for testing our software and for mapping candidate landing sites. Our initial tests focused on the Mars Pathfinder landing site because we had previously mapped parts of the region with both Viking Orbiter [*Howington-Kraus et al.*, 1995] and Mars Pathfinder IMP [*Kirk et al.*, 1999a] images, and for this work we used images identified in press releases on the Malin Space Science Systems (MSSS) website http://www.msss.com/mars_images/moc/index.html. Comparison of topography from MOC pairs immediately south of the landing point (MOC2-46; see *Kirk et al.* [2001]) and covering the landing point (MOC2-255) with one another and with other datasets provides a key validation of our methods.

Our first 4 stereopairs of candidate landing sites were obtained by an automated search of the cumulative index of MOC images that incorporated relatively crude criteria for image overlap and compatibility [*Kirk et al.*, 2002a]. Subsequent searches incorporating more accurate criteria, similar to those used in our search for Viking stereopairs [*Kirk et al.*, 1999b] are proving essential for locating images for scientific study planetwide, but the stereopairs of candidate landing sites described here were identified primarily by reference to the landing site maps prepared by T. Parker at JPL. Online versions of these maps (currently available at <http://marsoweb.nas.nasa.gov/landingsites/mer2003/topsites/final/>) provide hyperlinks to pages containing thumbnail views and geometric data for each image, so that potential pairs can be checked for suitability very efficiently. We occasionally received the latest versions of the maps from Parker (personal communications, 2001–2002) before the online maps were updated and

used the list of images at <http://marsoweb.nas.nasa.gov/landingsites/mer2003/mocs/> to access the thumbnail pages. The images were checked for noisy or dropped data, excessive atmospheric haze, and differences in illumination or surface albedo changes (mainly dust devil tracks) that would interfere with automatic stereomatching, and a preliminary check of stereo convergence was made by eliminating pairs in which both images had small emission angles. Positions of the MOC images in the landing site maps were determined interactively by Parker and we found them to be extremely accurate after THEMIS images became available and were incorporated in the maps (see figures in paper by *Golombek et al.* [2003, this issue]). Prior to the availability of THEMIS data, the MOC images were positioned with respect to a 231 m/pixel Viking mosaic base and their locations were less accurate, so that the extent of image overlap had to be assessed by inspection of the thumbnails.

In all, we identified more than 120 potentially useful images of the Mars Pathfinder site and 7 candidate MER sites. Many of these images (~30 pairs) were later eliminated, either after calibration in ISIS, at which time image quality and overlap could be assessed more accurately than by using the web pages, or after unsuccessful attempts at control and stereomatching. An additional 8 stereopairs of high quality were identified as "spares" but not mapped. We ultimately produced stereo DEMs from 22 pairs of images and generated photoclinometric DEMs in addition from images in 14 of these pairs. We also produced two clinometric DEMs in areas where stereo was not available, relying on alternate calibration approaches as described below. These images are summarized in Table 1. It is noteworthy that most of the images used have pixel sizes on the order of 3 m (the majority were obtained by 2x2 pixel summation), which is not as good as the best resolution of which the MOC-NA is capable, but better than the best

Viking Orbiter images and far superior to the best Viking coverage of the respective sites, which is typically 50–150 m/pixel.

2.3 Geodetic Control

Our experience with map-projecting and comparing MOC-NA and WA images indicates that errors of position (combining both spacecraft position and pointing errors) are often <100 m but occasionally greater, especially for off-nadir images. This is adequate to produce uncontrolled mosaics of WA images (≥ 240 m/pixel resolution) but inadequate for the higher resolution NA data. In particular, 100-m relative horizontal errors between images of a stereopair will give rise to comparable or greater vertical errors in the DEM. Because these errors are not strictly constant over the time of imaging, errors will also be introduced into the long-baseline slopes computed from an uncontrolled DEM. It is therefore highly desirable to use a bundle-adjustment process to bring the images into consistency with external control, even for slope studies and especially for scientific studies in which the high-resolution DEMs are to be compared and correlated with other datasets. This process is made challenging by the large gap in resolution between the NA images and the next-best datasets available for control. The MOLA dataset, with estimated absolute accuracies of <10 m vertically and ~100 m horizontally [Neumann *et al.*, 2001], is the ultimate source of control, but the spacing of MOLA footprints is hundreds to thousands of MOC-NA pixels. Direct comparison of the MOC images with MOLA profiles or gridded MOLA data is therefore helpful in bringing the stereomodels into vertical correspondence with the altimetry but less useful for improving their horizontal positioning. In our opinion, the best approach to refining the horizontal position of MOC-NA images and stereomodels would be to tie other images of intermediate resolution to the MOLA data and then

tie the MOC images to these. At the moment this usually means Viking Orbiter images, but over the next few years the visible-band camera of THEMIS will provide 18 m/pixel CCD frame images of much of Mars. We routinely use intermediate resolution frames to transfer control from MOLA in our stereomapping with Viking images [Rosiek *et al.*, 2001a], but we have yet to test the process with MOC data. The use of a large number of ties between intermediate-resolution images and MOC-NA will be essential to modeling and correcting the high-frequency oscillations of the MGS spacecraft with the advanced bundle-adjustment software we hope to develop. As discussed above, the bundle-adjustment capability currently available as part of SOCET SET does not include modeling of such high-frequency oscillations.

For the purposes of landing site selection (as opposed to precision landing), precise relative topographic data from which slope estimates can be made is more important than absolute accuracy. Our efforts to control the images listed in Table 1 have therefore focused mainly on bringing the stereomodels into vertical agreement with MOLA data. We begin by preparing a DEM of the region of interest from MOLA PEDR data [Smith *et al.*, 2001] at 250-m or 500-m grid spacing. The coordinate system uses the most recent set of Mars cartographic constants recommended by the International Astronomical Union and International Association of Geodesy [Duxbury *et al.*, 2002; Seidelmann *et al.*, 2002]. Similar products for the candidate MER landing sites are available online at <http://webgis.wr.usgs.gov/mer/>. In the fraction of cases where this MOLA DEM shows features that can also be identified in the images, we perform a preliminary adjustment to bring the nadir image into alignment with the MOLA data by means of along-track and across-track offsets to the spacecraft position. More often, no such features are visible and we simply freeze all orientation parameters for the nadir image. We next select a well-distributed set of points (typically 10–20) whose locations can be measured on both

MOC images. We then assign each point the elevation interpolated from the MOLA DEM at its *a priori* horizontal location. These heights are used as constraints in the main bundle-adjustment, but no constraints are placed on horizontal positions. The parameters adjusted in this calculation are corrections to the pointing angles of the off-nadir image, with the rotation around the boresight allowed to vary linearly with time and the remaining two angles allowed to vary quadratically. Our preliminary results for the first stereopair near the Mars Pathfinder landing site [Kirk *et al.*, 2001a] were based on a simpler control calculation using a single, loosely weighted MOLA elevation for all tiepoints in the plains. We have since regenerated this DEM with the control process described above.

Our attempts to control the stereopairs listed in Table 1 have been complicated by transmission errors in one or both of the images. It is a characteristic of the "packetized" transmission of image data to Earth that signal degradation between the spacecraft and ground station can cause the loss of blocks of image lines; if the degradation is extensive, it may not be known how many lines were lost [Malin and Edgett, 2001]. When this happens, the correct acquisition times of the lines after the gap (needed in sensor model calculations) are lost. For the time being our approach to working with MOC data after a data dropout is strictly empirical. We first compare the corrupted image with an uncorrupted image of the same region, estimate the number of missing lines, and insert this number of blank lines into the gap to approximately restore the image. We then control the image, being careful to place pass-points only in the section below the gap (if the section above the gap is needed for mapping, we treat it as an independent image) and allowing a larger than usual along-track adjustment of the spacecraft position to account for the error in reconstructing the gap size.

A final complication to the control process, encountered for most stereopairs (fortuitously, not for the first pair mapped at the Pathfinder site), arises from the high-frequency spacecraft pointing errors or "jitter" alluded to previously. Pointing oscillations in the direction of the stereobase (i.e., across-track for most MOC pairs) mimic elevation-related parallax and result in artifacts in the DEMs in the form of "stripes" elongated across-track. These artifacts are also reported by other users of MOC stereoimagery [*Ivanov and Lorre*, 2002; *Ivanov*, 2003; *Caplinger*, 2003] and have been described as giving the DEM a "washboard" appearance. From the dimensions of these DEM stripes we can infer the magnitude (highly variable but as much as 50 μ Rad or more than 10 MOC pixels) and frequency (1–4 Hz) of the oscillations that cause them. Smaller stripes in our DEMs are an artifact of the automatic matching algorithm and not the result of even higher frequency jitter as we previously reported [*Kirk et al.*, 2002b]. Oscillations of similar amplitude are seen in the spacecraft pointing data but the 2-second sampling interval of this dataset results in the jitter being aliased to much lower frequencies, so the pointing data are not useful for correcting the images. Jitter in the direction orthogonal to the stereobase (normally, along-track) results in localized mismatches between the images that confound both automatic and interactive DEM extraction. It is important to note that the likely magnitude of high-frequency pointing errors was known to MGS engineers (if not to users of the data) even before the mission. The MGS spacecraft was not specifically designed for high-resolution stereoimaging, and the MOC camera must share the platform with other instruments and articulated solar panels and high-gain antenna, all of which are sources of high-frequency vibration at a magnitude that does not impact the primary MOC goal of imaging for geologic interpretation.

The rigorous and therefore desired approach to correcting for these spacecraft pointing oscillations is to collect a dense set of tiepoints between the MOC stereoimages, intermediate-resolution frame images, and the MOLA DEM, and to perform a bundle-adjustment with specialized software that includes an appropriate parameterization of the high-frequency motion. Until such software is developed, we have been forced to develop alternative procedures to work around the problem. If the DEM can be collected, *ad hoc* processing to suppress the stripes in the direction of the parallax base is relatively straightforward. We first take the difference between the stereo-derived and MOLA DEMs at matching resolution, then apply a series of digital filters (lowpass boxcar filter across the image strip, followed by a highpass boxcar in the flight direction) to get an estimate of the "washboard" artifacts that can then be subtracted from the stereo DEM.

What is the influence of the "washboard" pattern on our slope estimates? With a characteristic amplitude of 50 m (peak-to-peak) and wavelength of 2 km, the washboard has maximum along-track slopes on the order of 5° . Examination of the DEMs before and after filtering suggests that, as a conservative estimate, the filtering process is at least 90% effective at removing the washboard pattern. Thus, errors in short-baseline along-track slopes after filtering are likely to be $<0.5^\circ$; as discussed below, this is less than the typical slope error due to imperfect stereomatching. The bidirectional slopes quoted in this paper are primarily measured in the across-track direction, however, and are essentially insensitive to jitter. Adirectional slopes, which combine along- and across-track slope components, will be affected to an intermediate extent.

The filtering also affects real topography to some extent and will suppress features (e.g., ridges) that cross all or most of the DEM. Again, only along-track slopes are affected. Low

spatial frequencies are preserved, because the MOLA component of the topography is not filtered. If the topography is isotropic, then features smaller than the width of the DEM are minimally affected as well. Most of our stereo DEMs are 2-3 km wide, comparable to the MOLA track spacing, so that all spatial frequencies are well preserved, but for narrower DEMs there will be a "gap" of intermediate spatial frequencies that will be affected. A few of our models (*e.g.*, Melas 2, Eos 2, Athabasca 2) are only about 1 km wide, and because of their narrowness the slope versus baseline behavior of these DEMs was evaluated along-track rather than across-track. We have assessed the effects of our filtering process on real topography by applying it to known, self-affine fractal DEMs (described in Section 3.2). In the worst case of a 1 km wide DEM, along-track slopes are reduced by about 10% of their true value at baselines of 10–1000 m, and no more than 20% of the true value at baselines of 1000–3000 m.

For stereopairs with severe jitter, it may be impossible to collect a DEM either automatically or interactively based on a single control solution with the existing software: if corresponding image lines are registered in one part of the pair, they may be so misaligned elsewhere that automatic stereomatching fails and the brain is incapable of fusing them in stereo. A few otherwise desirable stereopairs had such severe jitter that we were unable to produce a DEM, but in intermediate cases we found it useful to break the images into smaller sections and adjust the across-base orientation angle separately for each section. Sectional DEMs could then be collected, edited as usual, and merged. The resulting product is necessarily imperfect, as a continuous oscillation of the across-base angle has been corrected in a piecewise fashion, but the discontinuities in the DEM that result can be minimized. Needless to say, this process is undesirable both because it is extremely time-consuming and because it is approximate and necessarily subjective.

2.4 Photoclinometry

The two-dimensional photoclinometry (2D PC) algorithm developed by *Kirk* [1987] was used to produce DEMs of selected image areas at single-pixel post spacing, as opposed to the three-pixel spacing provided by stereo. A standalone (i.e., non-ISIS) software package embodying this algorithm was used to produce the majority of the photoclinometric DEMs described here and was also used to estimate the haze corrections, as well as to do slope-statistical analyses on the clinometric and stereo DEMs. This package can read image data from an ISIS-formatted file but does not make use of the image labels; instead, information such as the image resolution and illumination and viewing geometry must be entered manually. At the start of the work reported here, the photoclinometric part of the software also assumed that the image pixels were square. Early DEMs were therefore produced either from images that had been resampled to correct the pixel aspect ratio or from images that were map-projected (orthorectified) as part of the stereomapping process. Later DEMs were produced from geometrically raw (non aspect-corrected) images; these DEMs were aspect-corrected before slope analysis was performed. The geometric information derived from the cumulative index table and used in processing the non-projected images was probably accurate only to about 0.1° ; geometric information calculated for the images processed in map coordinates likely contained additional errors of $1\text{--}2^\circ$ because image skew was not accounted for. Since producing the DEMs described here, we have completed and released a set of ISIS programs for photoclinometry, as well as related tasks such as haze calibration and photometric parameter estimation [*Kirk et al.*, 2003a]. The photoclinometry programs obtain the needed geometric information directly from the image labels and from associated SPICE kernels and transform this information to the appropriate coordinate system (image coordinates or map coordinates, for both framing and

scanning cameras), thus avoiding the minor errors described above. The interactive photoclinometry program also presents a graphical user interface that simplifies the difficult process of controlling the iterative calculation. Further information about obtaining and using these ISIS photoclinometry programs is available online at <http://astrogeology.usgs.gov/Teams/Geomatics/pc.html>.

The photoclinometry algorithm can be summarized as the iterative, least squares adjustment of the DEM post elevations in order to make a shaded relief image calculated from the DEM fit the observed image. An important limitation of the method is that variations in surface reflectivity (albedo) are not generally accounted for in the shaded relief model. Areas of relatively constant albedo and images with relatively large incidence angles (so that contrast from topographic shading exceeds that from albedo variations) must therefore be selected for the results to be valid. Near-nadir images are also preferred because any parallax distortions in the image will be propagated into the coregistered DEM, though this is not a significant problem for the relatively flat sites considered here. Absolute radiometric calibration of the image is not required, but an accurate relative calibration is needed lest variations in camera sensitivity be mistaken for topographic effects. The relative calibration of the MOC narrow angle camera appears to be imperfect at about the 1% level. Bland images, including many used in this study, systematically appear to be slightly darker on their west side, leading to a gentle "crease" down the midline of many of our photoclinometric DEMs.

In order to obtain a quantitatively accurate DEM, it is necessary not only to calibrate the image and have an accurate photometric model (i.e., bidirectional reflectance function) for the surface [Kirk *et al.*, 2000b] but to account for light scattered in the atmosphere [Kirk *et. al.*, 2001b]. Unless the degree to which image contrast is reduced by atmospheric scattering is

correctly understood, the result will be a DEM with the correct qualitative shape but the wrong amplitude of relief, obviously useless for collecting slope statistics. A well-established approach to estimating the haze component of images for photoclinometry is to measure the brightness of a shadow and subtract this from the entire image. Unfortunately, the MOC orbit geometry precludes shadows in most images of the near-equatorial zone where the MER sites are located. We were able to use the shadow correction method for one nonstereo image (M07-01888 referred to as Athabasca 1) of Athabasca Vallis, which included a deep shadow in Cerberus Fossae. Using the radiance of a very deep shadow probably underestimates the haze radiance elsewhere in the image and therefore undercorrects the image slightly, resulting in the scale of relief, and hence the slopes, being underestimated by $\leq 15\%$ relative to their true values [*Kirk et al.*, 2001b]. Before usable stereo coverage of the Meridiani Planum "Hematite" site became available, we estimated the haze level for image E03-01763 (Meridiani 2 or Hematite 2) by requiring that dunes there have the same relative contrast after haze correction as dunes (with the same incidence angle and azimuth relative to the Sun) in other images for which the haze was estimated as described below. Since the opposing slopes on dunes are controlled by relatively universal physical processes [*Bagnold*, 1954], they should be similar from place to place on Mars and provide a convenient reference for image contrast.

The haze correction for the remaining images was determined by using alternative (and potentially more accurate) methods that we have developed to "calibrate" the photoclinometric DEM against an independent source of topographic data. These methods can be divided into inverse methods, where trial photoclinometry is performed and the haze correction is adjusted until the PC relief matches the independent source, and forward methods, in which the independent DEM is shaded and compared with the image. Which approach is preferred

depends on the *a priori* topographic data available, as well as on the geometric relation between topographic features and the illumination. The equatorial MER sites do not have the simple geometry (both illumination and MOLA profile crossing a well-defined topographic slope at large angles to the strike direction) that allowed us to adjust one-dimensional photoclinometric profiles to match individual MOLA profiles in the polar regions [Herkenhoff *et al.*, 1999; Soderblom *et al.*, 2002; Herkenhoff *et al.*, 2002], but an analogous, though slower, inverse calibration can be performed by using two-dimensional photoclinometry to produce a DEM and adjusting the haze to give agreement with an *a priori* DEM. In comparing the two DEMs, it is crucial to restrict attention to topographic features that are resolved in both. This can be done by comparing spot elevation differences or by performing a regression analysis, provided the region for the regression is carefully chosen. Use of a stereo-derived *a priori* DEM is also crucial, since the candidate landing sites were deliberately chosen to be flat and hence contain few topographic features resolved by MOLA. Forward calibration is carried out by simulating an image from the *a priori* DEM with a realistic surface scattering law but no atmospheric contribution. The intercept of a regression line relating the true image to the model is then the desired haze correction [Soderblom and Kirk, 2003]. Again, a stereo-derived DEM is preferred, and the region of comparison must be carefully chosen to contain well-resolved topographic features. Figure 1 illustrates the forward calibration of image E18-00196 in the Isidis site. Because of the severe jitter preventing automatic matching of the available stereopair, a DEM of a small but well-defined crater was produced interactively. The image shows several areas of high and low albedo not seen in the model shaded from the DEM, so the regression was performed on spot brightness measurements avoiding these areas. A formal error analysis of the fit indicates that the fractional uncertainty in the contrast in the image after haze correction, and hence the

fractional uncertainty in topography and slopes recovered by photoclinometry, is 13%. We have not performed error analyses for the height comparisons used in the inverse calibration, but the scatter in *a priori* and clinometric elevations is similar to the scatter in brightnesses shown in Fig. 1 so errors of no more than a few tens of percent are to be expected for this method as well. These error estimates are upper limits for the case where only a few reliable height or brightness measurements are available for calibration. In more favorable cases where the *a priori* DEM does a good job of resolving the topography [Soderblom *et al.*, 2002; Soderblom and Kirk, 2003] the calibration uncertainty may be a small fraction of a percent. As we will demonstrate below, other sources of error in slopes derived by photoclinometry are likely to be significantly smaller than the fractional error of 10-20% in the calibration for atmospheric haze.

The photometric behavior of the martian surface was represented in our analyses by a *Minnaert* [1941] function with limb-darkening parameter k determined separately at the phase angle of each image to mimic the behavior of the physically motivated but enormously more complex *Hapke* [1981; 1984; 1986] function as described by *McEwen* [1991]. The specific k values were obtained as described by *Kirk et al.* [2000b], but their impact on the results is minimal because the main effect of small variations in k is to alter the contrast of topographic shading. The calibration process thus corrects the effects of mis-estimation of k at the same time as it corrects for atmospheric haze. We have verified this assertion by calibrating one of the images and producing a DEM based on an erroneous value $k = 0.98$; the inferred haze differed from that for the correct value $k = 0.57$, but the DEM slopes were the same to a fractional accuracy of less than one percent. The surface photometric model will, of course, influence the results if the haze is determined from shadows or some other means rather than by calibration

against *a priori* topography. *Beyer et al.* [2003, this issue] show that the magnitude of this error is again likely to be no more than a few tens of percent of the true slope value.

3. Error Assessment

We have carried out an extensive series of tests with real and simulated data to assess the accuracy of elevations and particularly of slopes determined by stereo and photoclinometry. These tests also serve to introduce the techniques used below to characterize the slope statistics of the candidate MER landing sites.

3.1 Stereo Matching Errors

As noted above, MOC images SP1-23703 and SP1-25603 (referred to as MPF 1) were the first pair chosen for mapping because they cover an area near the Mars Pathfinder landing site for which other topographic datasets including "ground truth" were available for comparison. We present a statistical comparison of the slopes in the various datasets rather than a feature-by-feature comparison, both because of the disparate resolutions of the data sources and because this first MOC pair does not include the actual Pathfinder landing point. Figure 2 shows image SP1-23703, orthorectified, along with color shaded relief representations of both MOLA data and the stereo DEM for the same area. The low relief of this region is readily apparent: from the bottom to the top of Big Crater the total relief is 300 m. The unedited DEM is essentially free from artifacts. The high overall success of the SOCET SET matcher is gratifying, especially given the relatively low contrast of the images, because editing to correct matcher blunders is generally the most time-consuming and costly step of DEM production.

A portion of the stereomodel to the southwest of and excluding Big Crater was selected for statistical analysis to characterize the flat part of the landing site. Table 2 defines the region(s)

used for analysis in each DEM described in this paper, while slopes and other statistics are given in Table 3. The DEM in this area is consistent with our description based on Imager for Mars Pathfinder (IMP) data of the landing site topography as dominated by ridges and troughs with a typical amplitude of a few meters and a wavelength of several tens of meters [Kirk *et al.*, 1999a]. The smallest ridges are not fully resolved in the DEM but a pattern of somewhat larger ridges can be seen. Comparison of the image and DEM tends to support our previous assertion that many of the bright albedo features in the images are associated with local topographic highs. These are probably strips of light-colored, rock-free sediment similar to those seen (also along ridges) near the lander and interpreted as dunes by Greeley *et al.* [2000].

Figure 3 shows the distribution of bidirectional slopes derived from the plains area of the DEM in Fig. 2, for a north-south baseline of one post (approximately 12 m). The root-mean-squared (RMS) slope is 3.24° but, as the histogram shows, the slope distribution has longer tails (i.e., extreme slopes are relatively more common) than for a Gaussian distribution. Slopes on this baseline are in the range $\pm 11.31^\circ$ for 99% of the test area. For the adirectional slope (maximum slope in any direction, or gradient) over the same baseline, the 99th percentile is 14.57° .

It is also of interest to look at the RMS slopes over a variety of distance scales. Not only do slopes over long baselines and local slopes have different implications for landing safety, rover trafficability, and the geologic processes at work on the surface, but this type of analysis lets us compare the MOC DEM with other topographic datasets for the region. If $z(x)$ is a profile of height (relative to the local average, so that the average of z is 0) as a function of horizontal coordinate, and Δ is a horizontal baseline ("lag"), then the one-dimensional autocovariance function $\rho(\Delta)$ is given by

$$\rho(\Delta) = \langle z(x + \Delta)z(x) \rangle,$$

where the brackets $\langle \rangle$ indicate an ensemble average. The autocovariance is the inverse Fourier transform of the power spectral density, and for an ergodic function, the ensemble average can be approximated by a spatial average over both x and multiple parallel profiles, so that the inverse transform of an appropriate estimate of the power spectrum yields an estimate of the autocovariance [Oppenheim and Schaffer, 1975]. The Allan deviation ν , which is defined as the RMS difference in height between two points separated by a distance Δ [Shepard et al., 2001], can be expressed in terms of the autocovariance as

$$\nu(\Delta) = \sqrt{\langle \{z(x + \Delta) - z(x)\}^2 \rangle} = \sqrt{\langle z^2(x + \Delta) \rangle - 2\langle z(x + \Delta)z(x) \rangle + \langle z^2(x) \rangle} = \sqrt{2\{\rho(0) - \rho(\Delta)\}}$$

The RMS dimensionless (*i.e.*, rise/run) slope is then $s_{\text{RMS}} = \nu(\Delta)/\Delta$, and the RMS slope in angular units is $\Theta_{\text{RMS}} = \tan^{-1}(s_{\text{RMS}})$. The autocovariance, and hence the RMS slope as a function of baseline, can be obtained efficiently by fast Fourier transform techniques, but care is required because there are multiple approaches available for estimating the power spectral density. The periodogram (squared modulus of the Fourier transform of the profile, padded at the ends with zeros) yields an accurate estimate of the autocovariance when an inverse Fourier transform is applied [Oppenheim and Schaffer, 1975] but smoothed estimators of the power spectrum obtained by multiplying the profile by various "window" functions yield distorted versions of the autocovariance and hence inaccurate slope estimates. In our work, we extract profiles from the DEM, subtract the mean elevation of the region (rather than the mean of each profile), pad them

with a mirror image of themselves rather than with zeros, and average the squared modulus of the transform of multiple profiles to obtain the power spectral estimate. We have verified by extensive tests that this procedure yields RMS slope estimates in agreement with those obtained by direct calculation in the spatial domain, and it is substantially faster for large datasets. Note that no assumptions other than ergodicity about the topography are required; in particular, the topography need not be fractal for the calculation to be valid.

Figure 4 is a plot of RMS slope calculated by fast Fourier transform techniques for six independent DEMs covering different parts of the Mars Pathfinder landing ellipse at a variety of scales. Each of the curves shows a characteristic "dogleg" shape, with a steep section with RMS slope proportional to Δ^{-1} for large Δ and a shallower log-log slope at small Δ (the highest resolution dataset does not show an extended steep section but the beginning of a rolloff is nonetheless visible). Several factors contribute to the rolloff, the most important being edge effects that make the autocovariance and hence slope estimates increasingly inaccurate at large baselines. The scale at which edge effects become important depends somewhat on the data, but simulations indicate it is generally 10–20% of the horizontal size of the dataset. Detrending of the data has a similar impact on the slope curve and also tends to become important at 10–20% of the dataset length [Shepard *et al.*, 2001]. The simplified approach to control used for the Viking stereo and photoclinometry data [Howington-Kraus *et al.*, 1995], in which the whole DEM is tied to a single average elevation and regional slopes are not represented, is equivalent to detrending of the data and is probably responsible for the rollover at ~10% of the dataset length (~1 km). The rollover in the Viking photoclinometry data at ~4 km, however, represents a real change in the slope properties of the terrain, as the MOLA data show a corresponding break-point and this scale is only ~2% of the MOLA dataset width. As noted above, an early version

of our MOC stereo data [Kirk *et al.*, 2001a] was controlled in a way that effectively detrended it, but the version shown here was tied to MOLA at multiple points with differing elevations and hence has an accurate regional slope.

The similarity of the shallow portions of the slope curves at comparable baselines is striking, especially given that no two of these datasets cover precisely the same area, and supports the validity of our results. The MOLA dataset, extracted from the 64 pixel/degree EGDR gridded product [Smith *et al.*, 2001] covers a $2^\circ \times 2^\circ$ region approximately centered on the landing site. The photoclinometry data are taken from Viking image 004A72, which contains only smooth plains similar to those near the lander and south of Big Crater. The Viking stereo data cover the central, planar portion of the 100x200-km Pathfinder landing ellipse, excluding nearby rugged craters and streamlined islands [Howington-Kraus *et al.*, 1995] and agree well with the other results; stereo data from the full ellipse including more rugged features near the ends such as craters and streamlined islands yielded higher overall slopes as we previously reported [Kirk *et al.*, 2001a; 2002b] but a similar trend with baseline. The curve for IMP data is derived from a DEM extending 10 m on each side of the lander [Kirk *et al.*, 1999a] that was resampled from very irregularly spaced data. Slopes calculated directly from the unresampled datapoints by A. Haldemann [personal communication, 2003] agree well with those from the DEM, though they show more structure. Slope estimates over larger baselines can be computed from coarser IMP DEMs extending farther from the lander, but the RMS slope is systematically underestimated in these datasets, because much of the distant landing site was hidden behind ridges and the DEMs therefore contain (unrealistically) smooth patches interpolated from actual data for the visible areas. We have therefore not included these estimates in Fig. 4, but their lower RMS slopes are consistent with the value of 4.7° at 1-m baselines quoted by Kirk *et al.* [1999a].

There is no fundamental reason for the shape of the slope distribution to be independent of baseline, but it is likely that this assumption is at least approximately correct over modest baseline variations, and we have found in practice that slope distributions for many areas of Mars evaluated at various baselines—including all DEMs described in this paper—are always long-tailed. (Slope distributions from stereo typically have slightly longer tails than those from photoclinometry, perhaps reflecting blunders in the stereomatching process.) Because the distribution shape is unlikely to change greatly, the curves in Fig. 4 can also be used to scale estimates of percentile slopes measured at one baseline to a slightly different baseline. On this basis the 99th percentile adirectional slope for the MOC stereo DEM can be extrapolated to a baseline of 5 m, giving a value of 15.73°. The corresponding value for a second pair covering the landing point itself, discussed below, is 19.42°. Five meters is approximately the lengthscale at which the MER (and Pathfinder) airbag system "feels" the topography on which it lands, and consequently one simplified criterion for a safe landing site is a small (e.g., $\leq 1\%$) probability of encountering a slope in excess of 15° over this baseline.

The log-log slope of the curves in Fig. 4 can be interpreted in terms of fractal geometry [Turcotte, 1997]: if $s_{\text{RMS}}(\Delta) \propto \Delta^{H-1}$, where $0 \leq H \leq 1$ is the Hurst exponent, the fractal dimension of the surface is $D = 3 - H$. The MOLA, Viking stereo and photoclinometry and MOC stereo datasets show a similar dimension $D \sim 2.3$, whereas for the IMP data, $D \sim 2.4$. The transition occurs at a baseline near 10 m, which is roughly the wavelength of the system of ridges in the landing site. The change in Hurst exponents may thus reflect the structural features (fluvial or eolian ridges vs. rocks) that dominate relief at different scales, but it should be borne in mind that the slope estimates are also affected by the noise properties of the data and method used to produce the DEM. In any case, we find it interesting that a straight-line extrapolation of the

Viking curves from baselines ≥ 80 m, or even of the MOLA curve from 1–2 km baselines, yields slopes at centimeter scales that are within a factor of two of those measured *in situ*. Such near-constancy of the Hurst exponent over many orders of magnitude is definitely the exception rather than the rule, but this behavior at the Pathfinder site is clearly established by multiple datasets. Other DEMs described in this paper exhibit a variety of characteristics in their slope-baseline relations, such as single or multiple straight sections and even curved (nonfractal) sections. The values of the Hurst exponent, and the ranges of scales over which they apply, may provide clues to the geologic processes that shaped the terrains and are certainly superior to measures of the roughness at a single scale for characterizing the surface [Shepard *et al.*, 2001]. Unfortunately, a discussion of such characteristics of the candidate MER landing sites is beyond the scope of this paper. We limit our discussion of the MER mainly to slope estimates at the single baseline of 5 m and use the slope-baseline curve mainly to correct our results to this scale, *not* because we believe that this lengthscale fully characterizes the surface, but because of the MER safety criterion for slopes at 5 m baseline. Readers interested in roughness at other scales can obtain slope-baseline tables and slope probability distributions for all units (as well as the DEMs from which they were generated) at http://webgis.wr.usgs.gov/mer/moc_na_topography.htm.

Fig. 4 also contains data from a second MOC stereopair, M11-02414/E04-02227 (MPF 2). As seen in Figure 5, this pair extends northward from Big Crater and hence includes the actual Pathfinder landing point. It also overlaps the previously discussed pair MPF 1, allowing all four images to be controlled in a single adjustment calculation so that the DEMs register precisely. Slope statistics for the plains around the landing point, derived from this model, are consistent with both the earlier MOC model to the south and with the Pathfinder IMP data, though extreme slopes appear slightly more abundant. A direct comparison between the two MOC DEMs in

their area of overlap provides an indication of the errors in the stereomatching process, though this comparison is complicated somewhat by the systematic errors in the second DEM revealed in Fig. 5. In addition to the "washboard" pattern of ridges and troughs crossing the model, caused by spacecraft jitter, the DEM is systematically elevated along the edges relative to its midline. A similar pattern is seen in many MOC stereo DEMs, including those produced by other institutions [*Ivanov and Lorre, 2002; Ivanov, 2003; Caplinger, 2003*], with the edges sometimes elevated, sometimes depressed relative to the center. These artifacts result from uncorrected optical distortion in the MOC-NA camera. The amplitude of the topographic error depends on the distortion itself (which was found to be positive or pincushion, with a maximum amplitude of $\sim 1\%$ at the edges of the field of view), the stereo convergence angle, and the miss distance between the centerlines of the two images. Thus, MPF 1 (Fig. 2) was not visibly affected by this problem because the image tracks were fortuitously close together. The SOCET SET scanner sensor model is capable of correcting for known optical distortion, but, unfortunately, the DEMs presented here were all generated before the phenomenon was understood and they could not be regenerated and re-edited in the time available. To minimize the effect on slope estimates, stereo DEMs were generally rotated to align the ground track with the line axis and highpass filtered with a boxcar spanning the full along-track extent of the model, in order to remove the across-track curvature before calculating slopes.

The RMS deviation between the two MOC DEMs of the Pathfinder site, after filtering to suppress both jitter- and distortion-related artifacts, is 4.8 m. This height discrepancy can be used to estimate the stereomatching error, because it should equal the root-summed-square of the expected vertical precisions (EP) of the two pairs. The EP of a single stereopair is estimated as

$$EP = \Delta p \text{ IFOV} / (\text{parallax/height})$$

where IFOV is the instantaneous field of view of the image pixels in meters on the ground, the parallax/height ratio is calculated from the three-dimensional intersection geometry but reduces to $\tan(e)$ for an image with emission angle e paired with a nadir image, and Δp is the RMS stereomatching error in pixel units. By a simple statistical argument, if two images of differing IFOV are paired, the RMS of their IFOV values is used in the above equation. Applying this formulation to the two MOC pairs of the Pathfinder site, we estimate that $\Delta p = 0.30$ pixel. This value is slightly higher than the 0.2 pixel often used as a rule of thumb and confirmed with our matching software for several other planetary image datasets [Kirk *et al.*, 1999a; Howington-Kraus *et al.*, 2002b]. Other comparisons (below) give smaller values of Δp , so the matching error in this case may be increased by the blandness of the site and by the especially low contrast of the images in the first pair.

A similar analysis relating DEM differences to EP and thence to Δp may also be performed with independently produced DEMs from the same stereopair. We compared our DEM of pair E02-00270/E05-01626 (Melas 1) in Melas Chasma with corresponding models produced by Ivanov and Lorre [2002] and by the Harris Corporation for Malin Space Science Systems [Caplinger, 2003]. SOCET SET was used to resample the latter two DEMs via a seven-parameter transformation (translation, rotation, and isotropic scaling) to bring them into best registration with the USGS DEM. Elevation differences after this registration step were dominated by an along-track "arch" with an amplitude of a few tens of meters. This arch, as well as a slight side-to-side tilt in the difference DEMs, clearly results from the USGS model being controlled to MOLA with camera-angle adjustments allowed to vary quadratically with time as

described above, the other models being uncontrolled. Difference statistics were collected after highpass filtering with a boxcar the full width of the DEM and 50 lines high to remove the overall arch, and removing a handful of "blunders" (individual DEM posts with wildly discrepant heights) from the *Ivanov and Lorre* (JPL) model. The RMS difference between the USGS and Harris/MSSS models was 4.2 m, corresponding to $\Delta p = 0.22$ pixel provided the errors in the two matching algorithms are equal in magnitude and uncorrelated with one another. The RMS difference between the USGS and JPL models was only 1.8 m, strongly suggesting that the SOCET SET matcher used by USGS and the JPL matching algorithm are similar enough that they are subject to partially correlated errors. An alternative but much less likely explanation would require very small matching errors in the JPL dataset, intermediate errors of ~ 0.13 pixel in the USGS model, and large ~ 0.28 pixel errors for the Harris/MSSS model, all statistically independent from one another.

The USGS-JPL comparison raises some doubt about the assumption of independent errors in the USGS and Harris/MSSS DEMs. If these datasets also contain partially correlated errors, Δp might be greater than 0.22 pixel. We therefore carried out a final assessment of stereo matching errors specific to SOCET SET by using simulated data. The nadir image E02-00665 in Gusev crater was resampled by an affine transformation (translation, rotation, and anisotropic scaling) to register as closely as possible with its stereo partner E02-01453. The transformed nadir image was then input to SOCET SET as if it were actually the oblique image. In this way, we were able to simulate a stereopair with typical MOC imaging geometry and a range of surface textures typical for the Gusev site and the candidate MER sites as a whole, but with no local topographic parallax. Any deviations of the DEM recovered from this pseudo-stereo pair from a smooth surface could thus be attributed to matching error. The result obtained indicates $\Delta p = 0.22$ pixel,

supporting the assumption of equal and independent errors in the USGS and Harris/MSSS models and agreeing closely with the longstanding 0.2-pixel rule of thumb. Table 1 gives EP estimates calculated for each MOC pair by using $\Delta p = 0.22$ pixel. Values range from 0.8–5.8 m, with almost half between 1 and 2 m.

The spatial pattern of matcher errors revealed by this test is also of considerable interest, because it influences the error in slopes calculated from stereo data. As seen in Figure 6, the matching errors take the form of thin strips extending across the DEM, so that errors between points some distance apart are partially correlated. A similar error pattern can be seen superimposed on the real topography in smoother areas of many of our DEMs, so we believe this behavior is universal. Fourier analysis of the "slopes" that would be inferred from this erroneous "topography" indicates that the elevation errors become uncorrelated at across-track distances exceeding 81 DEM posts, and their correlation at smaller distances is approximately described by a Hurst exponent $H = 0.5$. This simple functional form allows us to predict the slope error σ_θ as a function of baseline Δ , ground sample distance (GSD) between DEM posts, and EP:

$$\sigma_\theta(\Delta) = \tan^{-1} \left(\frac{\sqrt{2}EP}{9GSD} \left(\frac{\Delta}{GSD} \right)^{-0.5} \right).$$

Note that if elevation errors were uncorrelated between DEM posts, the slope error would be a factor of 9 greater at the limit of resolution ($\Delta = GSD$), and would be proportional to Δ^{-1} . Stereo slope errors at the resolution limit, calculated by the above formula, are given for each model in Table 3. Values range from 0.7°–3.3° with the majority between 1°–2°. Slope errors at the limit of resolution are substantially smaller than the recovered RMS slope except in the Meridiani

Planum "Hematite" site, where the estimated slopes are comparable to or less than σ_θ by this formula, and the true stereo errors may be even greater, as discussed below. Because the $\Delta^{-0.5}$ dependence of the errors is steeper than the typical variation of the estimated slopes with baseline, the errors become increasingly unimportant at longer baselines.

3.2 Photoclinometry Simulations

The errors involved in the process of calibrating images for photoclinometry against a priori topographic data were discussed above. In order to assess some of the errors intrinsic to the clinometric method itself, we created a series of simulated images from known DEMs, then attempted to recover these DEMs by photoclinometry. Self-affine fractal topography [Turcotte, 1997] is convenient for such tests because it is easy to produce, contains roughness at a range of lengthscales, and its roughness can be controlled to crudely approximate the properties of various natural terrains [Shepard *et al.*, 2001; Shepard and Campbell, 1998]. We generated a series of random fractal DEMs with 1025x1025 posts, which we used to simulate 1024x1024 pixel images. The algorithm used to produce these models differs from the Fourier-filtering approach described by Turcotte [1997]. A series of DEMs of size 3x3, 5x5, 9x9, and so on, are filled with statistically independent "white" noise, interpolated to the full size of the desired DEM, scaled to give the desired power-law relation between relief and horizontal scale, and added together. Each DEM was also resampled to a 1024x1024 array of elevations at pixel centers for comparison with clinometric results in the same form. (As shown by Beyer *et al.* [2003, this issue], slopes measured between adjacent pixel centers will be less than slopes across individual pixels in the same model; our two-dimensional photoclinometry method returns the former whereas their point or "zero-dimensional" photoclinometry estimates the latter. Fortunately, the difference is much less significant for natural surfaces than for fractal models, which have significant pixel-

scale roughness.) Models were generated with Hurst exponents $H = 0.2, 0.5$, and 0.8 . Hurst exponents for our martian DEMs fall near the upper end of this range. The models were scaled to have a post spacing of 3 m and RMS slope of 1° between adjacent pixels. Versions of the $H = 0.8$ highpass and lowpass filtered at 16-pixel scale were also produced with the same scaling and hence somewhat smaller slopes at given baseline. An $H = 0.8$ model with 10° RMS slopes was also generated.

Images were then simulated from these DEMs, with an assumed emission angle of 0° , incidence angle of 45° , and Minnaert photometric model with $k = 0.72$, appropriate for Mars at this phase angle [Kirk *et al.*, 2000b]. For each model, images were produced both with illumination along the sample axis and at 22.5° (roughly typical of MOC images used in this study) to this axis. Photoclinometry was then performed on the synthetic images in a manner identical to that used for the MOC images. Figure 7 shows the image, the exact DEM, and the error in the clinometric DEM for a subset of cases. To characterize the original and photoclinometrically recovered DEMs, we calculated the RMS elevation, and RMS bidirectional slope in the sample direction, as well as the RMS error in photoclinometric topography and RMS clinometric slope, as summarized in Table 4. The raw RMS elevation errors are a substantial fraction of the relief, but it is evident from Fig. 7 that these errors, which essentially result from a lack of boundary conditions on the photoclinometric reconstruction, are far from random. They are almost entirely concentrated between, as opposed to along, profiles aligned with the sun, so that their impact on pixel-to-pixel slopes in the downsun direction or at small angles to this direction is minimized. The relative errors both for elevations along profiles and for slopes are typically $<1\%$ for the models with 1° nominal slope and $<10\%$ for models with 10° slope. Thus, if the surface and atmospheric photometric behavior are known perfectly (i.e., if the calibration process

were completely accurate) two-dimensional photoclinometry can be expected to give quite accurate slope estimates.

In addition to imperfectly corrected atmospheric haze, real images are subject to spatial variations of surface photometric properties ("albedo") that are not included in the clinometric modeling process at all. To get some idea of the impact of such albedo variations, we created an albedo map for our fractal terrains that mimicked some of the properties of small-scale albedo variations on the martian surface. The albedo distribution was obtained by stretching and clipping the highpass-filtered DEM, yielding a pattern in which local topographic minima are slightly darker than the rest of the surface. The pattern was then smoothed with a 2-pixel Gaussian filter, smeared slightly with the Adobe Photoshop "wind" filter, and scaled to have a RMS variation of 0.63% of the mean. This amplitude of albedo variation was chosen because it gives the same contrast variation that would be obtained from a (uniform albedo) surface with 0.5° RMS slope under the assumed illumination. Synthetic images of the unfiltered $H = 0.8$ surface with illumination azimuths of 0° , 22.5° , and 45° were multiplied by the albedo map and analyzed by photoclinometry. The results are summarized in Table 5 and Figure 8. In the case with illumination along the sample axis, the recovered RMS slope along this axis is increased from 1° to 1.12° , which is precisely what is expected if the real slopes and albedo-related "slopes" are independent (the albedo distribution is locally correlated with elevation, but not with slope) so that the corresponding variances add linearly: $\sqrt{1.0^2 + 0.5^2} = 1.12$. (*Beyer et al.* [2003, this issue] state the identical conclusion in terms of the slightly different slope values measured within rather than between pixels.) The albedo-related slope error increases dramatically with the angle between the illumination direction and slope baseline, however. This behavior results from the particular form taken by albedo-related artifacts. The photoclinometry algorithm

interprets each low-albedo patch on the surface as a region tilted away from the sun. To preserve continuity of the DEM, each such patch is joined by a ridge extending indefinitely on the upsun side and a trough on the downsun side. Similarly, bright patches would be tilted toward the sun and flanked by a trough and a ridge. These ridges and troughs have no effect on slopes in the illumination direction, but a strong effect on slopes at right angles to this direction. Fortunately, the pattern of stripes (ridges and troughs) can be strongly suppressed or even removed by appropriate spatial filtering of the DEM. The model must first be rotated so the stripes are aligned with the sample axis. Then an estimate of the stripes is generated by lowpass filtering the DEM along the sample direction and highpass filtering at right angles to isolate features with a particular minimum length and maximum width. This stripe estimate is then subtracted from the DEM, and the process is generally repeated to remove stripes of various sizes before re-rotating the model to its original orientation. Figure 9 shows the effects of such spatial filtering on the DEM recovered from one of our variable-albedo simulated images. As seen in Fig. 8, the filtering process does not entirely eliminate the slope error, but reduces the errors at all angles so that they are comparable to the error in slopes measured downsun.

The spatial filtering to remove stripes also affects some spatial-frequency components of the real topograph. Relief (ridges or troughs) that is highly elongated and aligned with the sun direction will be strongly suppressed, but the effect on slopes is minimal if the topography is close to isotropic. The filtering removes only components with high spatial frequency in the cross-sun direction and low spatial frequency downsun. As a result, slopes in the downsun direction are unaffected. Cross-sun slopes are reduced, but such slopes are poorly estimated by photoclinometry anyway, because the image contains little information about them. These assertions were verified by tests in which fractal topography with $H=0.8$, and an estimate of that

topography recovered by photoclinometry, were subjected to the destriping process. Downsun slopes were recovered almost perfectly by photoclinometry and were unaltered by filtering. Cross-sun slopes were underestimated by about 5% by photoclinometry and reduced an additional 10% by filtering. The apparent Hurst exponent for baselines from the minimum to 10% of the dataset width varied by less than 0.006 between the differently processed datasets.

From the foregoing simulations we can draw two useful conclusions about the errors that surface albedo variations may introduce into our slope estimates for candidate landing sites. First, because all DEMs were filtered to suppress albedo-related stripes before slope estimates were calculated, they do not contain the amplified slope errors seen in Fig. 8 for baselines crossing the illumination direction. Second, the magnitude of albedo variations and hence of slope artifacts will vary from region to region, but where the albedo variations contribute a small fraction of the total contrast in the image, they will contribute only minor errors to the slopes. Inspection of the MOC images indicates that albedo variations are small in relation to topographic contrast in all sites described here, with the exceptions of Mars Pathfinder and parts of Melas Chasma (where photoclinometry was not attempted) and Meridiani Planum. Photoclinometric slope results for Meridiani are likely to be mildly to severely corrupted by albedo variations and are thus upper limits on the actual slopes, but, despite this, the Meridiani site is clearly the smoothest studied.

4. Application to Candidate MER Landing Sites

We now describe the results obtained for the seven candidate landing sites mapped. A recurring theme is the determination of the most reliable and representative results for a given region: what spatial samples best characterize the range of hazards at the site, and, if both stereo

and photoclinometry results are available and give conflicting results, which should be believed? The answer to the former question comes from detailed mapping of the geomorphology of the sites, as described by *Golombek et al.* [this volume]. For the latter, photoclinometry will generally be preferred because of its superior resolution, the exceptions being if the site has highly variable albedo that would fool the method, or if the very computation-intensive photoclinometric method cannot be used to sample a large enough area to be truly representative.

4.1 Melas Chasma

The landing ellipse for this candidate site is located in Melas Chasma, in central Valles Marineris. The main target of scientific interest is what are believed to be lacustrine interior deposits [*Weitz et al.*, 2003, this issue]. These take the form of ovoid plateaux, up to several kilometers in length and 1 km in width. Part of the ellipse is also occupied by probable landslide materials, and a large portion is covered by finely spaced dunes. Three stereo DEMs sampling the dunes and interior deposits were generated (Figures 10–12), but the site was eliminated from consideration before additional pairs could be used to map the landslide deposits. Despite the early elimination of the site, the results obtained are worth discussing at some length because they illustrate the care that must be taken in interpreting stereo and photoclinometric DEMs. Slope statistics for the Melas 1 stereo DEM, areas *a–c* (Table 3) indicate a smooth surface, with area *b*, chosen to exclude the interior-deposit plateaux, being extremely smooth. What slopes are present mainly result from features several hundred meters or more across, as slopes on baselines shorter than this show very little variation (Figure 13). Close examination of the images, however, shows that the level and apparently featureless surfaces seen in Fig. 10 are covered by roughly north-aligned linear dunes (Figure 14). The spacing of the dunes ranges from ~10 m over much of the site to as much as 30 m. The results of photoclinometry suggest that the typical

height of the closely spaced dunes is 2–3 m, so that slopes approach 35° in places and the RMS adirectional slope exceeds 15° as shown in Table 3. Fourier analysis shows that the RMS slopes increase steadily from scales of hundreds of meters to about 10 m, consistent with the observed size of the dunes. Thus, the stereo DEM appears smooth because the only significant surface features smaller than 100 m across are too small to be resolved by the automatic matching algorithm. Each 3x3 matching neighborhood is about the same size (~ 10 m) as the dunes, and the recovered elevation is thus an average between the crests and troughs. Although the automatic algorithm failed to detect the dunes, we were able to make interactive spot measurements of elevations along the dune ridges and interdune troughs. Dune heights measured in this way were 2–3 m, confirming that the results of photoclinometry were accurate and not distorted by systematic albedo variations between the ridges and troughs or lee and stoss sides. The dune fields present an unappealing target for the MER mission: even if the landing were survivable despite the steep slopes, the rover would be condemned to a preordained traverse down the trough in which it ended up, with little view and less hope of traveling far enough to reach more interesting targets.

Melas stereomodels 2 and 3 covered more extensive interior deposits with only minor areas of dunes and confirmed that these deposits are nearly as rough as the dunes. As Figure 15 shows, the steep slopes are largely concentrated at the edges of the ovoid features, which are raised and generally quite level in their interiors. It is fortunate that the slopes are adequately resolved by stereo, because many (though not all) of the ovoids are significantly brighter than their surroundings, making photoclinometric mapping of them impossible.

The Melas site was eliminated after the 3rd MER Landing Site Workshop in 2002. The extreme roughness of the dunes and interior deposits was a significant contributing factor to this

decision, though the site was also judged unsafe based on the likelihood of high wind velocities [Rafkin *et al.*, 2003, this issue; Kass *et al.*, 2003, this issue].

4.2 Eos Chasma

The Eos site is also located in Valles Marineris and is of interest because of the possibility that it contains water-borne sediments [Greeley *et al.*, 2003b, this issue]. Two MOC stereopairs were analyzed in this area (Figures 16–17). Morphologically, the surface in the ellipse consists of cratered plains with hills ~100 m in height protruding from its surface. The apparent roughness of DEM subareas was a strong function of the fraction of their areas occupied by such hills, so that obtaining a properly representative sample of the site was the major concern. Had the site been one of the final four considered, it is likely that separate modeling of ridge and plains DEMs would have been combined with mapping to determine their relative areas, but Eos was eliminated after the 3rd Landing Site Workshop. As for Melas Chasma, winds were the main concern but the roughness of the terrain was also a factor in the elimination of the site.

4.3 Athabasca Vallis

The Athabasca site contains both a diversity of fresh volcanic features and evidence for catastrophic flooding originating in Cerberus Fossae [Burr *et al.*, 2002; Werner *et al.*, 2003, this issue]. The site was proposed relatively late, so MOC stereo coverage was not initially available, but we were able to calibrate photoclinometry on image M07-01888 (Athabasca 1) to the east of the ellipse by reference to shadows within Cerberus Fossae. DEMs of three image areas within the channel and similar to the terrain of interest in the ellipse itself (Figure 18) suggested that the surface is quite smooth. Subsequent analysis of stereopairs to the southeast of the ellipse and crossing its eastern tip yielded slope estimates that were greater but still probably safe based on the criterion of few 15° slopes. Both of these stereopairs had extremely narrow coverage, as

shown in Figures 19–20. The site was eliminated because of strong diffuse radar echoes, indicating that at least some terrains in the region have a high abundance of decimeter-sized rocks that would pose a hazard both for landing and for rover mobility [*Haldemann et al.*, 2003].

4.4 Isidis Planitia

The remaining sites discussed constitute the "final four" selected after the 3rd Landing Site Workshop in March 2002, from which the final MER A and B landing sites were picked in April 2003. The Isidis site is situated near the southern edge of that basin on materials believed to have been eroded from the ancient highlands of Libya Montes to the south [*Crumpler and Tanaka*, 2003, this issue]. The primary scientific interest of the site is thus the potential for sampling very ancient materials. The first stereopair mapped in this region (Figure 21) is in fact located ~150 km west of the ellipse in an alternative site previously eliminated, but the terrain sampled is generally similar to that within the ellipse. Slopes measured were intermediate to the range of results discussed so far, with the stereo results being preferred because photoclinometry was affected by localized dark deposits (mainly in crater floors). The first stereopair within the ellipse (Figure 22) covers a swarm of secondary craters with even more dramatic dark floor deposits, such that photoclinometry was not attempted. Out of concerns that this crater swarm might be rougher than the remainder of the ellipse, two more stereopairs were selected for analysis. Both were so severely affected by spacecraft jitter that it proved impossible to generate stereo DEMs, but interactive measurements were adequate to calibrate photoclinometry. For pair Isidis 4 this was done by forward fitting of a manual DEM of a single crater as described above (Fig. 1), whereas for Isidis 3 spot measurements of crater rim heights were used in the inverse fitting method. Photoclinometry was then applied to areas chosen to avoid the local dark deposits. The resulting slope estimates were similar to those from the other stereopairs. DEMs

of the secondary craters (from Isidis 2 stereo), cratered plains (Isidis 3 photoclinometry), and more heavily cratered plains (Isidis 4 photoclinometry) were chosen to characterize the hazard units at the site and supplied for simulation of the landing process. The hazard unit DEMs selected for Isidis and the remaining final four sites are indicated in Table 3; maps showing the locations of the hazard DEMs in relation to the landing ellipses and site geology are presented by *Golombek et al.* [2003, this issue]. The Isidis site was judged safe for the airbag system but was not selected because its scientific interest was less than that of Gusev and Hematite.

4.5 Elysium Planitia

The Elysium site, which is actually located in Utopia Planitia near the border with Elysium, was added for consideration relatively late in the selection process. The scientific rationale for this site is not as compelling as for some others [*Tanaka et al.*, 2003, this issue] but atmospheric models indicate that winds are likely to be safer than at the other sites [*Rafkin et al.*, 2003, this issue; *Kass et al.*, 2003, this issue]. The first stereopair analyzed (Figure 23) yielded relatively low slopes despite the presence of a wrinkle ridge and channel. These images showed both small bright dunes and diffuse albedo variations that prevented a satisfactory solution being obtained for the atmospheric haze level needed to calibrate photoclinometry. A second pair in more typical plains away from the wrinkle ridge (Figure 24) had even lower slopes determined from stereo. A satisfactory haze calibration was obtained from this stereo DEM and photoclinometry yielded slopes slightly greater than those from stereo (probably as a consequence of the dunes and other small albedo variations) but still quite small. The wrinkle ridge and plains were identified as separate hazard units for the purpose of landing simulations. The site was ultimately judged next in safety after Meridiani but not of the highest scientific interest, and was retained as an alternate.

4.6 Gusev Crater

The Gusev landing ellipse is morphologically the most complex of the final four, and its setting on the floor of the 160-km crater is arguably the most dramatic as well. The large valley network Ma'adim Vallis enters Gusev crater through a breach in the southern rim and continues through the low point on the northern rim, so the crater is likely to have been the site of a paleolake. If the lacustrine sediments are accessible to MER and not, for example, covered by more recent lavas, the scientific interest of the site would be exceptional [Cabrol *et al.*, 2003, this issue; Milam *et al.*, 2003, this issue]. This high interest, combined with the morphologic diversity of the site, led to the mapping of more MOC stereopairs here than at any other site. Somewhat surprisingly, the full range of surface textures was encountered in the very first pair (Figure 25), which included both very smooth cratered plains inside the 22-km diameter crater Thira at the extreme eastern end of the ellipse and much rougher knobby etched plains outside the ellipse to the south of Thira. Pair Gusev 2 sampled the knobby etched plains southwest of Thira but still outside the ellipse (Figure 26). The final pairs were situated within the ellipse, with Gusev 3 sampling typical cratered plains (Figure 27), adjacent pairs Gusev 4 and 5 sampling a small patch of etched plains associated with the ejecta of a 2-km crater (Figure 28), and Gusev 6 sampling a heavily cratered area, probably a cluster of secondary craters (Figure 29). The measured slopes spanned the range exhibited by the two terrains in Gusev 1, with intermediate values in areas (e.g., Gusev 4 a) containing both cratered and etched plains (Table 3). The heavily cratered region, in particular, was found to be no rougher than the "normal" cratered plains; it contains more, but not rougher, craters. All of the surfaces studied were covered almost uniformly with bright dust, so that photoclinometric analysis was highly successful. Several large, diffuse dark regions are present on the floor of Gusev within the ellipse, but, based on their

time variability and identical textures to neighboring bright areas, these are interpreted as regions where the bright dust has been removed by eolian activity [Greeley *et al.*, 2003a, this issue]. The dark areas were therefore not singled out for mapping as distinct hazard areas. The hazard unit DEMs selected at the site were, instead, cratered plains from Gusev 3, etched plains from Gusev 4/5, and heavily cratered plains from Gusev 6, all obtained by photoclinometry. The etched plains are rough and would not be safe to land on, but the area of such plains within the ellipse is small. Gusev was therefore judged safe overall and was selected as the MER B landing site in April 2003. Figure 30, though vertically exaggerated, gives an idea of the dramatic views that could be encountered if the rover lands near (but not in) the etched terrain. The rim of Gusev itself would appear equally dramatically from most locations in the ellipse.

4.7 Meridiani Planum "Hematite"

The Meridiani Planum site differs from the others in that its scientific interest comes not from morphologic evidence of water, but from the spectroscopic detection by the TES instrument of crystalline hematite [Christensen *et al.*, 2000], a mineral that may have been deposited by hydrothermal activity [Baldridge *et al.*, 2003, this issue; Allen *et al.*, 2003, this issue]. The site itself is thus referred to as "Hematite" both informally and in our previous publications [Kirk *et al.*, 2002a; 2002b]. It is clearly the smoothest site studied and has as a result been the most difficult to map. The early stereopairs Meridiani (Hematite) 1 and 3 were investigated intensively enough to be numbered as such, but were dropped when it proved impossible to obtain valid results from such bland images by automatic stereomatching; they do not appear in Tables 1–3. (For these images, the SOCET SET matcher produced, not the error pattern visualized in Fig. 6, but Maltese-cross shaped artifacts with an amplitude exceeding 100 m and bounded by near-vertical cliffs.)

In the absence of useful stereo coverage, we applied photoclinometry to image E03-01763. Because no clear shadows could be found in this or neighboring images, we modeled the haze in the images by requiring that the contrast between opposite sides of the dunes commonly found in crater bottoms be similar (after haze subtraction) to the contrast of dunes in the Melas 1 pair. Illumination conditions for the Melas and Meridiani images were similar, both sets of dunes were oriented similarly to the sun, and their slopes may be expected to be similar on physical principles [Bagnold, 1954]. Radiative-transfer modeling [Kirk *et al.*, 2001b] indicated that the haze radiance obtained in this way corresponded to an optical depth of 0.4, within the range inferred for other images calibrated against stereo DEM data. The maximum and minimum possible haze radiances (equal to the darkest image pixel and to zero, respectively [Beyer *et al.*, 2003, this issue]) would yield slope estimates a factor of 2.4 greater or smaller respectively than our best estimate.

The images of the Meridiani site display few obvious topographic features but prominent albedo variations. We selected three subareas for analysis that sampled most of the range of albedo and topography in the site (Figure 31). Area *a* contains especially prominent albedo variations in the form of "curdled" patterns of small bright patches. Such patches are especially common around the rims of subdued craters, which often have diffuse dark deposits in their interiors. Area *b* is more typical of the site, being blander, with a few small pits and other topographic features but still mainly albedo variations. Area *c* contains more rugged areas that appear to outcrop from the smooth plains. Photoclinometric slopes can be expected to contain almost entirely albedo-related artifacts in area *a*, and a mixture of albedo effects and true topography in areas *b* and *c*. The latter areas had some of the lowest slopes in our study, while even the purely albedo-related "slopes" in area *a* were intermediate and would only be

marginally unsafe if real. These results were thus reassuring on some level, yet unsatisfying given the lengthy chain of argument involved and the contamination of real slopes by artifacts.

Two usable stereopairs were subsequently obtained and mapped, each containing typical bland plains and one or more subdued impact craters (Figures 32–33). Slopes inferred from these stereomodels were highly consistent with the photoclinometric slopes (excluding area *a*; see Table 3) in the plains and slightly greater for the craters taken by themselves. Close examination of the shaded relief shows that the texture of the stereo DEMs in the plains exhibits no noticeable correspondence to the images and hence is likely to be the result of stereomatching errors. The RMS slopes inferred from the stereo DEMs outside the craters are also slightly smaller than the predicted slope errors. The stereo results, like those from photoclinometry, are thus likely to be only an upper limit on the slopes. The large crater and an area of plains were selected from the Meridiani/Hematite 4 stereo DEM as the best representations of the range of slope hazards at the site. Not surprisingly, the site was determined to be safe, and it was chosen as the prime target for MER A.

5. Conclusions

We have shown that stereo and photoclinometric techniques can be applied to MOC-NA images to map topography at scales of 3–10 m/post and estimate slopes with a relative accuracy of 10–20%. This level of accuracy is more than adequate to discriminate between the hazard units identified photogeologically in the candidate landing sites for MER, which have RMS bidirectional slopes in the range $\sim 1^\circ$ – 10° . Our early determination that steep slopes are pervasive in Melas and Eos Chasmata was a contributing factor, albeit a minor one, in the elimination of these candidate sites, and the rough terrain sampled in Gusev crater was

worrisome. More extensive mapping has shown that the sites finally chosen, and, indeed, all of the final four sites, are likely to be safe as far as 5-m scale slopes are concerned. Only Gusev contains extremely rough terrains, and these occupy such a limited area of the landing error ellipse that they are not of major concern. The other chosen site, Meridiani, is not only the smoothest surface studied, but so smooth that measuring its relief posed a serious challenge. Figures 34–36 show images, color shaded relief topography, and adirectional roughness for the 9 type localities selected to represent hazard units in the final sites, and Figs. 37–38 summarize the roughness properties of these regions.

More generally, the newly developed software and techniques reported here are opening a door to a new realm of Mars topography. The ability to produce DEMs with horizontal resolutions of 10 m and better from MOC images will be invaluable for selecting future landing sites and will no doubt contribute significantly to the study of a wide variety of surface processes. These capabilities will also be almost immediately applicable to analyzing medium- to high-resolution stereoimagery from scanning cameras on current and future missions such as 2001 Mars Odyssey, Mars Express and Mars Reconnaissance Orbiter.

6. Acknowledgements

We thank Tim Parker, Mike Caplinger, Anton Ivanov, and Albert Haldemann for supplying their data for use in this paper. The MOC team is particularly to be thanked for their pre-release of images of the candidate landing sites to support the mapping and selection process. We are also grateful to the members of the MER Landing Site Selection Committee for their encouragement and specifically for their aid in prioritizing images for study. Thanks to Ken Tanaka, Ken Herkenhoff, Tom Duxbury, and Bruce Campbell for helpful review comments.

Development of the software used in this project was funded by the NASA Planetary Geology and Geophysics Planetary Cartography program (NASA contract W-18,777). Mapping of the landing sites was performed under funding from the MER mission (Cornell contract 39361-6499) and the Mars Fundamental Research Program (NASA contract W-10,251).

7. References

- Albertz, J., et al., The camera experiments HRSC and WAOSS on the Mars 94 mission, *Int. Arch. Photogramm. Remote Sens.*, 29(B1), 130–137, 1992.
- Allen, C., et al., Potential for Astrobiology Investigation of the Hematite Site, *J. Geophys. Res.*, 2003, this issue.
- Anderson, F. S., et al., MOLA topography and slopes of MOC images in the MER landing site, *J. Geophys. Res.*, 2003, this issue.
- Bagnold, F. R. S., *The physics of blown sand and desert dunes*, Methuen, New York, 1954.
- Baldrige, et al., Hydration state of the martian hematite exposures: Implications for their origin and evolution, *J. Geophys. Res.*, 2003, this issue.
- Beyer, R. A., A. S. McEwen, and R. L. Kirk, Meter-scale slopes of candidate MER landing sites from point photoclinometry, *J. Geophys. Res.*, 2003, this issue.
- Burr, D. M., J. A. Grier, A. S. McEwen, and L. P. Keszthelyi, Repeated aqueous flooding from the Cerberus Fossae: Evidence for very recently extant, deep groundwater on Mars, *Icarus*, 159, 53–73, 2002.
- Cabrol, N., et al., MER A in Gusev crater: Testing hypotheses with the Athena payload, *J. Geophys. Res.*, 2003, this issue.
- Caplinger, M., Mass production of DEMs from MOC stereopairs, ISPRS-ET Working Group IV/9 Workshop "Advances in Planetary Mapping 2003", online at http://astrogeology.usgs.gov/Projects/ISPRS/MEETINGS/Houston2003/abstracts/Caplinger_isprs_mar03.pdf, 2003.
- Caplinger, M. A., and M. C. Malin, The Mars Orbiter Camera geodesy campaign, *J. Geophys. Res.*, 106(E10), 23,595–23,606, 2001.

- Christensen, P., et al., The Thermal Emission Imaging System (THEMIS) instrument for the 2001 Orbiter, *Lunar Planet. Sci.*, XXX, Abstract #1470, Lunar and Planetary Institute, Houston (CD-ROM), 1999.
- Christensen, P., et al., Detection of crystalline hematite mineralization on Mars by the Thermal Emission Spectrometer: Evidence for near-surface water. *J. Geophys. Res.*, 105(E4), 9623–9642, 2000.
- Cook, A. C., et al., Clementine imagery: selenographic coverage for cartographic and scientific use, *Planet. Space Sci.*, 44(10), 1135–1148, 1996.
- Crumpler, L., and K. Tanaka, Geology and MER target sites along the southern rim of Isidis Planitia, Mars, *J. Geophys. Res.*, 2003, this issue.
- Duxbury, T. C., R. L. Kirk, B. A. Archinal, and G. A. Neumann, Mars Geodesy/Cartography working Group recommendations on Mars cartographic constants and coordinate systems. *Int. Arch. Photogramm. Remote Sens.*, XXXIV(4), "Geospatial Theory, Processing and Applications", Ottawa (CD-ROM), 2002.
- Eliason, E., Production of digital image models using the ISIS system. *Lunar Planet. Sci.*, XXVIII, 331–332, Lunar and Planetary Institute, Houston, 1997.
- Gaddis, L. et al., An overview of the Integrated Software for Imaging Spectrometers (ISIS), *Lunar Planet. Sci.*, XXVIII, 387–388, Lunar and Planetary Institute, Houston, 1997.
- Golombek, M. P., et al., Selection of the Mars Exploration Rover landing sites, *J. Geophys. Res.*, 2003, this issue.
- Greeley, R., et al., Wind-related features in Gusev crater, Mars, *J. Geophys. Res.*, 2003a, this issue.

- Greeley, R., et al., Eos Chasma, Mars: A potential landing site for astrobiology, *J. Geophys. Res.*, 2003b, this issue.
- Greeley, R., Draft, J. D., Kuzmin, R. O., and Bridges, N. T., Mars Pathfinder landing site: Evidence for a change in wind regime from lander and orbiter data, *J. Geophys. Res.*, 105, 1829–1840, 2000.
- Haldemann, A. F., and F. S. Anderson, Mars Exploration Rover landing site hectometer slopes, *Eos Trans. AGU*, 83(47), Fall Meet. Suppl., Abstract P22-A-0390, 2002.
- Haldemann, A. F., et al., Radar properties of the proposed Mars Exploration Rover landing sites, *J. Geophys. Res.*, submitted, 2003.
- Hapke, B. W., Bidirectional reflectance spectroscopy 1: Theory, *J. Geophys. Res.*, 86, 3039–3054, 1981
- Hapke, B., Bidirectional reflectance spectroscopy 3: Corrections for macroscopic roughness, *Icarus*, 59, 41–59, 1984.
- Hapke, B., Bidirectional reflectance spectroscopy 4: The extinction coefficient and the opposition effect, *Icarus*, 67, 264–280, 1986.
- Herkenhoff, K. E., N. T. Bridges, and R. L. Kirk, Geologic studies of the Mars Surveyor 1998 landing area, *Lunar Planet. Sci.*, XXX, Abstract #1120, Lunar and Planetary Institute, Houston (CD-ROM), 1999.
- Herkenhoff, K. E., L. A. Soderblom, and R. L. Kirk, MOC photoclinometry of the North Polar Residual Cap, *Lunar Planet Sci.*, XXXIII, Abstract #1714, Lunar and Planetary Institute, Houston (CD-ROM), 2002.
- Howington-Kraus, E., R. Kirk, D. Galuszka, T. Hare, and B. Redding, Validation of the USGS sensor model for topographic mapping of Venus using Magellan radar stereoimagery, *Lunar*

- Planet. Sci.*, XXXIII, Abstract #1986, Lunar and Planetary Institute, Houston (CD-ROM), 2002a.
- Howington-Kraus, E., L. Soderblom, R. Kirk, B. Giese, and J. Oberst, USGS and DLR topographic mapping of Comet Borrelly, *Int. Arch. Photogramm. Remote Sens.*, XXXIV(4), "Geospatial Theory, Processing and Applications", Ottawa (CD-ROM), 2002b.
- Howington-Kraus, E., R. L. Kirk, B. Redding, and L. A. Soderblom, High-resolution topographic map of the Ares-Tiu landing site from Viking Orbiter data, In: *Mars Pathfinder Landing Site Workshop II, LPI Tech. Rep. 95-01*, 38–39, 1995.; map reproduced in Tanaka, K. L., Sedimentary History and mass flow structures of Chryse and Acidalia Planitia, Mars, *J. Geophys. Res.*, 102, 4131–4149, 1997.
- Ivanov, A. B., Ten-meter scale topography and roughness of Mars Exploration Rovers landing sites and Mars polar regions, *Lunar Planet. Sci.*, XXXIV, Abstract #2084, Lunar and Planetary Institute, Houston (CD-ROM), 2003.
- Ivanov, A. B., and J. J. Lorre, Analysis of Mars Orbiter Camera stereo pairs, *Lunar Planet. Sci.*, XXXIII, Abstract #1845, Lunar and Planetary Institute, Houston (CD-ROM), 2002.
- Kass, D., et al., Analysis of atmospheric mesoscale models for entry, descent, and landing, *J. Geophys. Res.*, 2003, this issue.
- Kirk, R. L., III. *A fast finite-element algorithm for two-dimensional photogrammetry*, Ph.D. Thesis (unpubl.), Caltech, 165–258, 1987.
- Kirk., R. L., et al., Digital photogrammetric analysis of the IMP camera images: Mapping the Mars Pathfinder landing site in three dimensions, *J. Geophys. Res.*, 104(E4), 8869–8887, 1999a.

- Kirk, R. L., J. Barrett, and E. Howington-Kraus, A database of Viking Orbiter image coverage for cartographic and scientific use, *Lunar Planet. Sci.*, XXX, Abstract #1857, Lunar and Planetary Institute, Houston (CD-ROM), 1999b.
- Kirk, R. L., J. M. Barrett, and L. A. Soderblom, Photoclinometry made simple...? ISPRS-ET Working Group IV/9 Workshop "Advances in Planetary Mapping 2003", online at http://astrogeology.usgs.gov/Projects/ISPRS/MEETINGS/Houston2003/abstracts/Kirk_isprs_mar03.pdf, 2003a.
- Kirk, R. L., E. Howington-Kraus, and B. Archinal, High Resolution Digital Elevation Models of Mars from MOC Narrow Angle Stereoimages. ISPRS-ET Working Group IV/9 Workshop "Planetary Mapping 2001", online at http://astrogeology.usgs.gov/Projects/ISPRS/MEETINGS/Flagstaff2001/abstracts/Isprs_etm_OCT01_kirk_mars_moc_stereo.pdf, 2001a.
- Kirk, R. L., E. Howington-Kraus, and B. Archinal, Topographic analysis of candidate Mars Exploration Rover landing sites from MOC Narrow-Angle stereoimages, *Lunar Planet. Sci.*, XXXIII, Abstract #1988, Lunar and Planetary Institute, Houston (CD-ROM), 2002.
- Kirk, R. L., E. Howington-Kraus, B. Redding, D. Galuszka, T. Hare, and B. A. Archinal, High-resolution topomapping of candidate MER landing sites with MOC: New results and error analyses, *Lunar Planet. Sci.*, XXXIV, Abstract #1966, Lunar and Planetary Institute, Houston (CD-ROM), 2003b.
- Kirk, R. L., E. Howington-Kraus, and M. Rosiek, Recent planetary topographic mapping at the USGS, Flagstaff: Moon, Mars, Venus, and beyond, *Int. Arch. Photogramm. Remote Sens.*, XXXIII(B4), 476 (CD-ROM), 2000a.

- Kirk, R. L., L. A. Soderblom, E. Howington-Kraus, and B. A. Archinal, USGS high resolution topomapping of Mars with Mars Orbiter Camera Narrow-Angle images. *Int. Arch. Photogramm. Remote Sens.*, XXXIV(4), "Geospatial Theory, Processing and Applications", Ottawa (CD-ROM), 2002.
- Kirk, R. L., K. T. Thompson, T. L. Becker, and E. M. Lee, Photometric modeling for planetary cartography, *Lunar Planet. Sci.*, XXXI, Abstract #2025, Lunar and Planetary Institute, Houston (CD-ROM), 2000b.
- Kirk, R. L., K. T. Thompson, and E. M. Lee, Photometry of the martian atmosphere: An improved practical model for cartography and photoclinometry, *Lunar Planet. Sci.*, XXXII, Abstract #1874, Lunar and Planetary Institute, Houston (CD-ROM), 2001b.
- Malin, M. C., et al., Mars Observer Camera, *J. Geophys. Res.*, 97, 7699–7718, 1992.
- Malin, M. C., et al., Early views of the martian surface from the Mars Orbiter Camera of Mars Global Surveyor, *Science*, 279, 1681–1685, 1998.
- Malin, M. C., and K. S. Edgett, Mars Global Surveyor Mars Orbiter Camera: Interplanetary cruise through primary mission, *J. Geophys. Res.*, 106(E10) 23,429–23,570, 2001.
- McEwen, A. S., Photometric functions for photoclinometry and other applications, *Icarus*, 92, 298–311, 1991.
- McEwen, A. S., et al., HiRISE: The High Resolution Imaging Science Experiment for Mars Reconnaissance Orbiter, *Lunar Planet. Sci.*, XXXIII, Abstract #1163, Lunar and Planetary Institute, Houston (CD-ROM), 2002.
- Milam, K., et al., THEMIS Characterization of the Gusev Landing Site, *J. Geophys. Res.*, 2003, this issue.

- Miller, S.B. and A. S. Walker, Further developments of Leica digital photogrammetric systems by Helava, *ACSM/ASPRS Annual Convention and Exposition Technical Papers*, 3, 256–263, 1993.
- Miller, S. B. and A. S. Walker, Die Entwicklung der digitalen photogrammetrischen Systeme von Leica und Helava, *Z. Photogramm. Fernerkundung*, 1(95), 4–16, 1995.
- Minnaert, M., The reciprocity principle in lunar photometry, *Astrophys. J.*, 93, 403–410, 1941.
- Neumann, G. A., D. D. Rowlands, F. G. Lemoine, D. E. Smith, and M. T. Zuber, The crossover analysis of Mars Orbiter Laser Altimeter data, *J. Geophys. Res.*, 106(E10) 23,753–23,768, 2001.
- Oppenheim, A. V., and R. W. Schaffer, *Digital Signal Processing*, Prentice-Hall, Englewood, New Jersey, 532–571, 1975,
- Rafkin, S., et al., MRAMS mesoscale model results for MER, *J. Geophys. Res.*, 2003, this issue.
- Rosiek, M. R., R. Kirk., T. Hare, and E. Howington-Kraus, Utilizing Mars Digital Image Model (MDIM) and Mars Orbiter Laser Altimeter (MOLA) data for photogrammetric control, ISPRS-ET Working Group IV/9 Workshop "Planetary Mapping 2001", online at http://astrogeology.usgs.gov/Projects/ISPRS/MEETINGS/Flagstaff2001/abstracts/isprs_etm_OCT01_rosiek_mars_photogrammetry.pdf, 2001a.
- Rosiek, M. R., R. Kirk., T. Hare, and E. Howington-Kraus, Combining lunar photogrammetric topographic data with Clementine LIDAR data. ISPRS-ET Working Group IV/9 Workshop "Planetary Mapping 2001", online at http://astrogeology.usgs.gov/Projects/ISPRS/MEETINGS/Flagstaff2001/abstracts/isprs_etm_OCT01_rosiek_moon_topography.pdf, 2001b.

- Seidelmann, P. K., et al., Report of the IAU/IAG working group on cartographic coordinates and rotational elements of the planets and satellites: 2000, *Celest. Mech. Dyn. Astron.*, 82, 83–110, 2002.
- Shepard, M. K., and B. A. Campbell, Shadows on a planetary surface and implications for photometric roughness, *Icarus*, 134, 279–291, 1998.
- Shepard, M. K., et al., The roughness of natural terrain: A planetary and remote sensing perspective, *J. Geophys. Res.*, 106(E12), pp. 32,777–32,795, 2001.
- Smith, D. E., et al., The global topography of Mars and implications for surface evolution, *Science*, 284, 1495–1503, 1999.
- Smith, D. E., et al., Mars Orbiter Laser Altimeter: Experiment summary after the first year of global mapping of Mars, *J. Geophys. Res.*, 106(E10), 23,689–23,722, 2001.
- Soderblom, L. A., and R. L. Kirk, Meter-scale 3D models of the martian surface from combining MOC and MOLA data, *Lunar Planet. Sci.*, XXXIV, Abstract #1730, Lunar and Planetary Institute, Houston (CD-ROM), 2003.
- Soderblom, L. A., R. L. Kirk., and K. E. Herkenhoff, Accurate fine-scale topographic profiles in the martian south polar region from MOLA-Calibrated photometric modeling of MOC NA images, *Lunar Planet. Sci.* XXXIII, Abstract #1254, Lunar and Planetary Institute, Houston (CD-ROM), 2002.
- Tanaka, K., et al. Geology of the MER 2003 "Elysium" candidate landing site in southeastern Utopia Planitia, Mars, *J. Geophys. Res.*, 2003, this issue.
- Torson, J. and K. Becker, ISIS: A software architecture for processing planetary images, *Lunar Planet. Sci.*, XXVIII, 1443-1444, Lunar and Planetary Institute, Houston, 1997.

Turcotte, D. L., *Fractals and Chaos in Geology and Geophysics*, Cambridge Univ. Press, New York, 1997.

Weitz, C., et al., Melas Chasma as a candidate landing site for MER, *J. Geophys. Res.*, this issue, 2003.

Werner, S. C., et al., Continual geologic activity in Athabasca Valles, *J. Geophys. Res.*, 2003, this issue.

Zuber, M. T., et al., The Mars Observer Laser Altimeter investigation, *J. Geophys. Res.*, 97, 7781–7797, 1992.

8. Figure Captions

Figure 1. Scatterplot (cross-histogram) of image radiance vs. model from DEM provides an important check on quality of fit for haze. (a) Portion of MOC image E18-00196 showing ~400-m crater in Isidis Planitia. Crosses mark locations of manual sampling of radiance, avoiding localized bright and dark patches. (b) Corresponding portion of model image created by shading stereo DEM. (c) Scatterplot of image radiance vs. model radiance. Data for all pixels (points) show scatter due to albedo variations and limited resolution. Data for manually sampled points (crosses) are better correlated, allowing fitting of regression line whose intercept is desired haze radiance. Fractional uncertainty in intercept of regression, 13%, equals fractional uncertainty in photoclinometric slopes.

Figure 2. First MOC-NA stereopair processed (referred to as MPF 1) comprises images SP1-23703 and SP1-25603, covering "Big Crater" near Mars Pathfinder landing site and plains to S and W but unfortunately not the landing site itself. Left to right, orthorectified image SP1-23703, color shaded relief from MOLA data (the two MOLA profiles in this area miss Big Crater, which therefore does not appear), color shaded relief from MOC stereo. Total relief from floor to rim of Big Crater is 300 m. Automatic stereomatching was entirely successful, with no blunders detectable in the DEM.

Figure 3. Histogram of bidirectional slopes over a 1-post (12 m) N-S baseline from the portion of the MOC DEM near Big Crater seen in Fig. 4. Gaussian distribution with the same RMS slope (4.2°) as observed is shown for comparison. Large slopes are significantly more common than the Gaussian model would suggest.

Figure 4. RMS slopes of regions near Mars Pathfinder landing site calculated as described in text from DEMs based on images of a variety of scales and sources. MOLA data are

extracted from the 64 pixel/degree EGDR and cover a $2^{\circ} \times 2^{\circ}$ region containing the Pathfinder landing ellipse. VO stereo DEM covers only the central part of ellipse (excluding high-relief features) and was interpolated from contours obtained by analytic photogrammetry of 38 m/pixel Viking images. VO photoclinometry DEM was obtained from 38 m/pixel image 004A72 of smoothest part of landing ellipse, highpass filtered to suppress artifacts of photoclinometry. MOC stereo DEM derivation is reported here. IMP stereo DEM covers the region from the lander to 10 m at ground sample distance (GSD) of 2 cm, and was interpolated from data collected on IMP stereopairs with highly variable ground spacing. Slope data computed by A. Haldemann directly from the irregularly spaced IMP datapoints without resampling generally agree with those from resampled IMP data. Slopes over smaller baselines for each DEM are expected to be most accurate and are consistent between datasets. Slopes at longest baselines for each dataset are affected by boundary effects and the control process and systematically underestimate real slopes.

Figure 5. MOC stereopair M11-02414/E04-02227 of the Mars Pathfinder landing site (MPF 2). Landing point is in approximate center of the image, ~2 km north of Big Crater. Orthoimage and color shaded relief MOLA and MOC DEMs are as in Fig. 2; fourth image shows MOC DEM after filtering to suppress "washboard" artifacts due to spacecraft jitter. Artifact (depressed centerline and raised edges) due to optical distortion remains. Comparison of overlap area between MPF 1 and MPF 2 DEMs after filtering to suppress both jitter and distortion errors can be used to assess stereomatching errors and DEM accuracy as described in text.

Figure 6. Grayscale representation of part of a DEM obtained by matching MOC image E02-00665 with a copy of itself transformed to agree in position, orientation, and scaling with

stereo image E02-0453. As this synthetic stereo pair contains no local topographic parallax, contents of the DEM reflect matching errors for realistic martian surface texture at MOC resolutions. Inferred RMS matching error is 0.22 pixel.

Figure 7. Use of synthetic self-affine fractal terrains to evaluate errors in photoclinometry. Left to right: fractal terrain with Hurst exponent $H=0.8$, same terrain lowpass filtered, highpass filtered at 16 pixel cutoff. Top: synthetic images of terrains, with illumination direction 22.5° anticlockwise from sample axis. Middle: perspective views of terrains with vertical exaggeration 10. Bottom: perspective views of error in DEMs reconstructed from images by photoclinometry. Vertical exaggeration 10 for full fractal and lowpass-filtered cases, 100 for highpass-filtered case. Error is nearly constant along downsun profiles, leading to minimal impact on slopes measured downsun or at low angles to sun.

Figure 8. Fractal terrain used to illustrate effect of spatially varying albedo on photoclinometry. Left: image of fractal terrain (cf. Fig. 7) with albedo having RMS variations equal to 0.63% of mean. Ratio of albedo to topographic contrast exceeds that typical of candidate landing site images used in this study; image has been contrast enhanced. Middle: grayscale representation of DEM produced by photoclinometry. "Stripes" (ridges and troughs) along sun direction, caused by albedo features are evident. Right: same DEM after filtering to suppress sun-aligned stripes.

Figure 9. Sensitivity to albedo variations of slopes from photoclinometry depends on azimuth. Synthetic fractal images (cf. Fig. 8, left) were generated with various illumination directions and analyzed by photoclinometry. Error in raw clinometric DEM increases markedly as slope baseline cuts characteristic stripe artifacts (Fig. 8, center) at increasing angles.

Filtering DEM to suppress stripes (Fig. 8, right) does not eliminate errors entirely but reduces errors at all azimuths to be comparable to those in downsun direction.

Figure 10. MOC stereopair E02-00270/E05-01626 (Melas 1), presented as in Fig. 5. Ovoid plateaux of interior deposits, which extend laterally across much of the DEM at top, have also been partially suppressed by the filters used to remove "washboard" artifacts.

Figure 11. MOC stereopair M08-04367/E09-02618 (Melas 2). Inset shows relation of DEM area shown to larger area of stereo overlap, northern portion of which was not mapped because it consists of dunes similar to Melas 1.

Figure 12. MOC stereopair M04-00361/E12-00720 (Melas 3). Spacecraft was relatively stable during acquisition of these images, so filtering to suppress "washboard" artifacts was not needed.

Figure 13. RMS slopes in a dune-covered region of Melas Chasma (Melas 1 stereomodel E02-00270/E05-01626, Fig. 10) as a function of baseline; compare Fig. 6 for the Pathfinder landing site. Stereo DEM gives low slopes with little variation at baselines <100 m, suggesting that the site is extremely smooth, but photoclinometry reveals that dunes unresolved by the stereomatcher are much rougher. Figure also shows that stereo and photoclinometric DEMs can be merged to combine the absolute accuracy at long-baselines of the former with the high spatial resolution of the latter. (Curve for the merged DEM shows slightly lower slopes than for pure photoclinometry DEM at short baselines because it covers a larger area including some dune-free regions.) Slopes for interior deposits from Melas 2 and 3 stereo DEMs (Figs. 11–12), which contain roughness at a much wider range of scale, are also shown.

Figure 14. Enlargement of dunes in 5.5x6.9 km subarea of Melas 1 (Fig. 10). Left: orthoimage showing bright dunes on interior deposit plateau at top and surrounding canyon floor. Center: grayscale representation of stereo DEM of same area. Canyon floor appears smooth. Right: grayscale representation of merged stereo and photoclinometric DEM of same area, resolving topography of dunes. Grayscale covers same 60-m elevation range for both DEMs.

Figure 15. Perspective view of Melas 3 stereo DEM (Fig. 12), seen from the southwest with vertical exaggeration of 4. Orthoimage has been draped over the DEM and colored with adirectional slope. Red color indicates slopes $\geq 15^\circ$, primarily at the edges of ovoid plateaux of interior deposits. Dunes appear smooth (purple to blue, indicating slopes $\leq 5^\circ$) at the limited resolution of the stereo DEM but see Figs. 13–14.

Figure 16. MOC stereopair E02-02855/E04-01275 (Eos 1).

Figure 17. MOC stereopair E04-02155/E11-02980 (Eos 2).

Figure 18. Subareas of MOC image M07-01855 (Athabasca 1 *a*, *b*, *c*) selected for photoclinometric processing, showing range of textures similar to those in landing ellipse. Haze calibration for these images was obtained from a deep shadow within Cerberus Fossae included in the same image. Systematic difference in tone between left and right sides of image areas *b* and *c* is interpreted as a $<1\%$ residual error in radiometric calibration, as the same pattern is seen in multiple images (cf. Fig. 34). This error introduces erroneous long-baseline slopes into the photoclinometric DEM.

Figure 19. MOC stereopair M07-05928/E10-02604 (Athabasca 2). Stereo overlap area is narrow but a well-defined crater feature can be used to calibrate haze level for photoclinometry.

Figure 20. MOC stereopair M07-00614/E05-00197 (Athabasca 3).

Figure 21. MOC stereopair E02-02016/E02-01301 (Isidis 1). Datasets are interrupted by region of dropped data. Control adjustment and collection of stereo DEM were carried out separately for segments before and after gap, as discussed in text. Area shown is ~150 km west of landing ellipse.

Figure 22. MOC stereopair E13-00965/E14-01522 (Isidis 2). High quality of stereo data is fortunate, given dark crater floors that prevent use of photoclinometry.

Figure 23. MOC stereopair E18-00429/E21-00118 (Elysium 1).

Figure 24. MOC stereopair E22-00379/E18-01455 (Elysium 2).

Figure 25. MOC stereopair E02-00665/E02-01453 (Gusev 1).

Figure 26. MOC stereopair E01-00341/E05-00471 (Gusev 2). Datasets are interrupted by region of dropped data.

Figure 27. MOC stereopair M03-01042/E17-01547 (Gusev 3).

Figure 28. Adjacent MOC stereopairs E18-00184/E17-00827 (Gusev 4) and E05-03287/E18-00184 (Gusev 5). Only Gusev 5 DEM required filtering to suppress "washboard" artifact. Image E18-00184, shared by these pairs, was used for photoclinometry.

Figure 29. MOC stereopair E19-00218/E21-00256 (Gusev 6).

Figure 30. Perspective view of region of knobby etched plains in image E18-00184 near the center of the Gusev landing ellipse (see Fig. 28). Topographic data from photoclinometry at 3.13 m/pixel with vertical exaggeration ~7. A portion of the rim of a 2-km crater is seen on the horizon, with ejecta occupying part of the foreground. Color is artificial, intended to suggest that of the martian surface.

Figure 31. Subareas of MOC image E03-01763 (Meridiani/Hematite 2 *a*, *b*, *c*) selected for photoclinometric processing. Subarea *a* shows "curdled" bright and diffuse dark albedo

markings with only minor topographic features (pits) identifiable. Subarea *b* is more representative of landing site, with blander appearance but albedo variations still dominating topographic shading. Subarea *c* shows rougher material appearing to protrude through smooth plains, but still contains substantial albedo variations. Slopes inferred from *a* thus are almost entirely fictitious. Slopes from *b* and *c* are upper limits on true slopes because of significant albedo-related artifacts, yet are among the smoothest for any location studied.

Figure 32. MOC stereopair E12-03255/E18-01595 (Meridiani/Hematite 4). Note lack of correlation between texture of plains in shaded relief and in image, indicating that stereo slopes for plains are likely dominated by stereomatching errors rather than real relief. Raised center of DEM is an artifact due to uncorrected optical distortion and was removed by highpass filtering before slope analysis.

Figure 33. MOC stereopair E15-00023/E21-01653 (Meridiani/Hematite 5).

Figure 34. Images of the 9 areas chosen as representative of hazard units mapped at the final four candidate landing sites appear at common scale but with independent contrast stretches to maximize visibility of features in each. Systematic difference in apparent brightness between the two sides of many of the images appears to be a <1% residual error in radiometric calibration. (a) Elysium plains; (b) Elysium ridge; (c) Gusev cratered plains; (d) Gusev etched plains; (e) Gusev heavily cratered plains; (f) Isidis heavily cratered plains; (g) Isidis cratered plains; (h) Isidis secondaries; (i) Meridiani plains; (j) Meridiani subdued crater.

Figure 35. Color shaded relief of 9 hazard unit DEMs appear with independent contrast stretches and elevation intervals colored to maximize visibility of features in each; see Fig. 36 to compare roughness of units. Apparent valley along the centerline of most photoclinometric

DEMs is the result of residual calibration error. Units are lettered as in Fig. 34. Data sources (ST=stereo, PC=photoclinometry) and elevation intervals from purple to red are as follows: (a) PC, 90 m; (b) ST, 120 m; (c) PC, 40 m; (d) PC, 200 m; (e) PC, 40 m; (f) PC, 40 m; (g) PC, 60 m; (h) ST, 50 m; (i) ST, 30 m; (j) ST, 60 m.

Figure 36. Color-coded adirectional slope maps of 9 hazard unit DEMs. Consistent coloring from purple (0°) to red (20°) as shown by colorbar is used to facilitate comparison. Units are lettered as in Fig. 34.

Figure 37. Plot of RMS bidirectional slope as a function of baseline for the 9 hazard unit DEMs in the final four candidate landing sites shown in Figs. 34–36. Curves are labeled to correspond to areas a–j in Figs. 34–36.

Figure 38. Cumulative probability distributions for adirectional slopes of the 9 hazard units in the final four sites. Curves are labeled to correspond to areas a–j in Figs. 34–36. Curves indicate the probability of encountering slopes less than or equal to the indicated value. The slope-versus-baseline behavior shown in Fig. 37 has been used to adjust the distribution determined at the resolution of each DEM to 5-m baseline for comparison between units and with the sensitivity of the MER landing system to slopes $\geq 15^\circ$ at this scale.

9. Tables

Table 1. MOC Images Used

Site	Set ^a	Lon ^{b,c}	Lat ^{b,c}	Image 1	Image 2	Res 1 ^d	Res 2 ^d	Ema 1 ^{b,e}	Ema 2 ^{b,e}	Stereo Angle ^{b,f}	EP (m) ^g	Stereo DEM ^h	PC DEM ^h
Pathfinder	1	326.7	19.2	SP1-23703	SP1-25603	2.55	3.23	21.37	30.67	19.3	1.7	√	
	2	326.8	19.3	M11-02414	E04-02227	1.58	1.85	14.09	26.37	12.3	1.6	√	
Melas	1	282.3	-8.7	E02-00270	E05-01626	2.88	3.01	0.22	12.78	12.8	2.9	x	√
	2	281.8	-8.7	M08-04367	E09-02618	2.84	3.01	0.21	18.09	18.1	2.0	√	
	3	282.5	-8.6	M04-00361	E12-00720	2.85	3.01	0.20	17.94	17.9	2.0	√	
Eos	1	318.7	-13.4	E02-02855	E04-01275	4.30	3.30	0.19	21.90	21.9	2.1	√	√
	2	318.2	-13.4	E04-02155	E11-02980	2.87	3.00	0.16	17.97	18.0	2.0	√	√
Athabasca	1	156.8	9.9	M07-01888		5.87		0.10					√
	2	155.6	8.1	M07-05928	E10-02604	5.85	6.18	0.09	17.98	18.0	4.2	x	
	3	156.1	9.2	M07-00614	E05-00197	5.87	6.61	0.10	19.21	19.2	4.0	√	√
Isidis	1	84.9	4.6	E02-02016	E02-01301	2.93	3.08	0.16	12.99	13.0	2.9	x	x
	2	88.9	4.3	E13-00965	E14-01522	2.92	3.06	1.16	18.05	18.1	2.1	HU	
	3	87.9	4.3	E22-00281	E20-01635	2.99	3.28	9.93	19.87	29.8	1.3		HU
	4	88.7	4.4	E02-00049	E18-00196	5.86	3.06	0.00	18.06	18.1	3.2		HU
Elysium	1	124.4	11.8	E18-00429	E21-00118	3.10	3.55	17.97	24.74	32.4	1.3	HU	
	2	123.8	11.6	E22-00379	E18-01455	3.65	4.19	26.77	33.73	60.5	0.8	√	HU
Gusev	1	176.1	-14.8	E02-00665	E02-01453	2.87	3.32	0.23	22.12	22.1	1.7	√	√
	2	175.9	-15.0	E01-00341	E05-00471	2.85	2.96	0.07	9.99	10.0	3.7	√	√
	3	175.0	-14.7	M03-01042	E17-01547	7.09	2.96	0.19	11.82	11.8	5.8	x	HU
	4	175.3	-14.6	E18-00184	E17-00827	3.15	3.67	18.33	29.06	10.7	3.4	√	HU
	5	175.4	-14.7	E05-03287	E18-00184	2.85	3.15	0.02	18.33	18.3	2.0	√	
	6	175.2	-14.7	E19-00218	E21-00256	2.85	2.94	0.12	10.28	10.3	3.6	√	HU
Meridiani ^j	2	253.3	-2.3	E03-01763		2.90		0.24					√
	4	354.1	-2.2	E12-03255	E18-01595	3.01	4.00	11.04	32.47	21.2	1.8	HU	
	5	354.6	-1.9	E15-00023	E21-01653	3.04	3.58	17.9	26.66	29.4	1.3	√	

^aPairs or single images for photoclinoetry used were numbered sequentially within sites; Meridiani 1 and 3 are omitted because stereo processing was unsuccessful. ^bAll angles in degrees. ^cApproximate east longitude, planetocentric latitude at DEM center. ^dCross-track pixel dimension in m. ^eEmission angle. Image with lowest emission angle listed first in each pair. ^fConvergence angle, allowing for 3D stereo geometry. ^gExpected vertical precision of stereo, based on 0.22 pixel matching error; see text. ^h√ indicates reliable DEM obtained by this method; x indicates DEM judged less reliable or representative than from other method or other sets in site; HU indicates reliable DEM chosen to represent a hazard unit mapped at the site for landing safety simulations. See text. ^jAlso known informally as "Hematite".

Table 2. DEM Subareas Analyzed

Site	Set	Sub Area	Used for ^a	Dataset Geometry ^b	Start Samp	End Samp	Start Line	End Line
MPF	1	a	ST-slopes	Map	101	356	32	665
MPF	2	a	ST-slopes	Map	76	203	201	456
Melas	1	a	ST-slopes	Map	92	243	16	750
		b	ST-slopes	Map	178	340	751	1485
		c	ST-slopes	Map	178	243	16	1485
		d	ST+PC	Ortho	351	900	1501	2300
		e	PC-slopes	Ortho	881	1009	1901	2156
Melas	2	a	ST-slopes	Map, rot 7.54°	427	516	2001	3200
Melas	3	a	ST-slopes	Map	80	208	155	577
Eos	1	na	ST-fit haze	Map	157	352	764	1047
		nb	ST-fit haze	Map	71	290	296	404
		nc	ST-slopes	Map	185	313	461	1280
		nd	PC-slopes	Ortho	381	1070	1901	2500
Eos	2	a	ST-slopes	Map, rot 7.33°	351	440	51	2550
		b	ST-fit haze	Map, rot 7.33°	351	440	471	620
		c	PC-slopes	Image ^c	1	512	1025	1536
		d	PC-slopes	Image ^c	1	512	2301	2812
Athabasca	1	a	PC-slopes	Image	1	512	12601	13112
		b	PC-slopes	Image	1	512	11571	12082
		c	PC-slopes	Image	25	512	10601	11112
Athabasca	2	n	ST-slopes	Map, rot 7.56°	372	427	389	901
Athabasca	3	a	ST-slopes	Map, rot 6.59°	524	652	2500	3850
		b	ST-fit haze	Map, rot 6.59°	544	633	2261	2510
		c	PC-slopes	Image	1	512	4801	5312
		d	PC-slopes	Image	1	512	3801	4312
Isidis	1	na	ST-fit haze	Map	76	285	18	517
		nb	ST-slopes	Map	145	285	18	1047
		nc	PC-slopes	Ortho	301	1100	1201	2100
		sa	ST-slopes	Map	172	300	65	1264
		sb	PC-slopes	Ortho	401	1200	2151	2850
Isidis	2	a	ST-slopes	Map, rot 7.48°	168	274	16	1278
Isidis	3	a	ST-fit haze	Image ^d	1	1024	4392	4992
		b	PC-slopes	Image	1	1024	1801	1350
Isidis	4	a	ST-fit haze	Map ^e				
		b	PC-slopes	Image	325	1024	2475	4224
Elysium	1	a	ST-slopes	Map, rot 7.53°	172	459	45	1293
Elysium	2	a	ST-slopes	Map, rot 6.56°	163	327	21	1370
		b	ST-fit haze	Map	226	310	1305	1354
		c	PC-slopes	Image	1	1024	201	1224
		d	PC-slopes	Image	1	1024	2401	3424
Gusev	1	a	ST-slopes	Map	92	244	1	650
		b	ST-fit haze	Map	153	326	621	400
		c	ST-slopes	Map	256	384	1071	2047
		d	PC-slopes	Ortho	236	821	351	1615
		e	PC-slopes	Ortho	641	1240	3551	5150
Gusev	2	a	ST-slopes	Map	99	273	20	665
		b	ST-slopes	Map	198	347	728	1457
		c	PC-slopes	Ortho	319	915	51	2200
		d	PC-slopes	Ortho	648	1160	2401	4800
Gusev	3	a	ST-fit haze	Map	161	327	1201	1450
		b	ST-slopes	Map, rot 7.32°	287	414	51	1200
		c	PC-slopes	Ortho ^f	3725	4236	301	3600
Gusev	4	a	ST-slopes	Map, rot 6.53°	209	408	274	1808
		b	ST-fit haze	Map	155	314	941	1280
		c	PC-slopes	Image	1	1024	901	2500
Gusev	5	a	ST-slopes	Map, rot 7.41°	240	301	901	1220
Gusev	6	a	ST-slopes	Map, rot 7.68°	235	437	32	1733
		b	ST-fit haze	Map	171	330	901	1220
		c	PC-slopes	Image	1	1024	1701	3500
Meridiani	2	a	PC-slopes	Image	1	512	6001	6513
		b	PC-slopes	Image	1	257	7781	8293
		c	PC-slopes	Image	256	512	4291	4803
Meridiani	4	a	ST-slopes	Map, rot 7.35°	150	429	41	1175
		b	ST-slopes	Map, rot 7.35°	150	429	451	1175
		c	ST-slopes	Map, rot 7.35°	210	429	231	450

Meridiani	5	a	ST-slopes	Map, rot 7.38°	200	482	41	1549
-----------	---	---	-----------	----------------	-----	-----	----	------

^aST=stereo, PC=photoclinometry, used to measure slope statistics or calibrate haze for photoclinometry. ^bCoordinate system in which subarea is defined: Image=raw image geometry; Ortho=orthorectified image in cylindrical projection at ~1-pixel (3.0 or 6.0 m) spacing; Map=cylindrical projection at ~3-pixel (10.0 or 20.0 m) spacing; some map datasets rotated clockwise by angle indicated to align stereo overlap region with line-sample grid. Ortho and Map datasets are shown in Figs. 2, etc. ^cAspect-corrected and 2x2 averaged before processing. ^dSevere jitter; photoclinometry on indicated area calibrated against spot heights collected by interactive stereo. ^eSevere jitter; stereo DEM of small crater (Fig. 1) collected manually and used for haze calibration. ^fIndicated area was resampled to 6m/pix by 2x2 averaging before processing.

Table 3. Slope Statistics

Site	Set	Sub Area	DEM from ^a	Baseline (m)	Stereo Slope Error ^{b,c}	RMS Bidir Slope ^{b,d}	RMS Adir Slope ^{b,e}	99% Adir Slope ^{b,e}	Slope Correction to 5 m Base ^f	99% Adir Slope@ 5 m ^b	P(Adir≥15°) @ 5 m	Remarks ^g	Hazard Unit
MPF	1	a	ST	10	1.50	3.24	4.50	14.57	1.086	15.73	0.012	SW of Big Crater, no jitter	
MPF	2	a	ST	10	1.42	3.26	4.72	17.80	1.098	19.42	0.019	Landing site, filt for jitter	
Melas	1	a	ST	10	2.63	2.71	4.856	14.05	1.000	14.05	0.008	Does not resolve dunes	
		b	ST	10	2.63	1.55	2.66	7.69	1.000	7.69	<0.001	"	
		c	ST	10	2.63	2.42	4.10	12.41	1.000	12.41	0.004	"	
		e	PC	3		12.97	15.46	35.83	0.923	33.67	0.289	Dunes resolved!	
Melas	2	a	ST	10	1.81	9.86	12.68	37.16	1.187	41.96	0.233	Layers	
Melas	3	a	ST	10	1.83	11.22	14.08	43.20	1.273	50.09	0.274	"	
Eos	1	nc	ST	10	1.93	6.24	9.14	30.97	1.092	33.24	0.072		
		nd	PC	3		5.80	7.04	22.30	0.927	21.83	0.029	PC area misses hills	
Eos	2	a	ST	10	1.83	6.03	7.92	23.79	1.189	27.66	0.087		
		c	PC	5.74		8.05	9.52	26.21	1.005	26.31	0.082		
		d	PC	5.74		10.46	13.56	31.71	1.005	31.83	0.239	PC area dominated by hills	
Athabasca	1	a	PC	5.87		1.26	1.72	5.01	1.020	5.11	<0.001	NE of ellipse but similar	
		b	PC	5.87		0.94	1.48	3.76	1.057	3.96	<0.001	"	
		c	PC	5.87		1.25	1.86	4.84	1.019	4.98	<0.001	"	
Athabasca	2	n	ST	20	1.88	3.39	4.71	15.30	1.125	17.11	0.019	S of ellipse, higher standing	
Athabasca	3	a	ST	20	1.82	2.48	3.45	10.09	1.409	11.48	0.004		
		c	PC	5.87		3.98	5.33	13.53	1.007	13.62	0.006		
		d	PC	5.87		2.66	3.48	8.44	1.010	8.52	0.001		
Isidis	1	nb	ST	10	2.64	4.65	6.37	24.07	1.202	28.24	0.037	Far outside ellipse	
		nc	PC	3		5.68	7.41	21.28	0.983	20.94	0.027	"	
		sa	ST	10		4.11	5.78	19.31	1.058	20.34	0.027	"	
		sb	PC	3		8.43	10.65	28.55	0.987	28.24	0.121	"	
Isidis	2	a	ST	10	1.86	5.84	8.83	26.18	1.033	26.92	0.088	Dark floored secondary ctrs	Isidis Secondaries
Isidis	3	b	PC	2.99		2.43	3.13	9.80	0.977	9.58	0.003	Cratered plains	Isidis Crplains
Isidis	4	b	PC	3.06		3.36	4.52	15.53	0.991	15.41	0.012	Heavily cratered plains	Isidis Heavy Crplains
Elysium	1	a	ST	10	1.13	3.51	5.06	13.16	1.016	13.37	0.006	Wrinkle ridge	Elysium Ridge
Elysium	2	a	ST	10	0.68	1.92	2.74	8.20	1.038	8.51	0.001	Plains	
		c	PC	3.29		3.18	4.06	9.72	0.981	9.53	0.003	"	Elysium Plains
		d	PC	3.29		3.50	4.41	11.71	0.983	11.52	0.003	"	
Gusev	1	a	ST	10	1.55	2.79	4.92	15.87	1.076	17.01	0.015	Cratered pl in Thira	
		c	ST	10	1.55	5.62	8.15	23.53	1.066	24.91	0.078	Knobby etched S of Thira	
		d	PC	3		4.19	5.21	14.96	0.982	14.70	0.010	Cratered pl in Thira	
		e	PC	3		9.27	11.51	29.41	0.990	29.16	0.163	Knobby etched pl S of Thira	
Gusev	2	a	ST	10	3.34	8.26	11.22	33.26	1.048	33.12	0.157	Knobby etched pl SW of Thira	
		b	ST	10	3.34	12.55	16.08	40.05	1.049	41.40	0.340	"	
		c	PC	3		8.93	11.49	28.26	0.989	27.99	0.166	"	
		d	PC	3		12.05	15.53	36.88	0.985	42.42	0.299	"	
Gusev	3	b	ST	10	2.63	9.33	12.76	34.55	1.114	37.50	0.233	Smooth pl in ellipse center	
		c	PC	6		3.04	4.07	13.25	1.006	13.32	0.007	Preferred due to jitter in ST	Gusev Crplains
Gusev	4	a	ST	10	3.09	4.44	6.13	17.94	1.064	19.02	0.028	Mix of etched, cratered plains	
		c	PC	3.13		8.08	10.24	27.96	0.994	27.82	0.047	Etched plains and ejecta	Gusev Etched
Gusev	5	a	ST	10	1.84	8.26	11.00	31.13	1.200	35.92	0.195	Etched plains and ejecta	

Gusev	6	a	ST	10	3.23	2.26	4.21	9.67	1.035	10.00	0.002	Heavily cratered plains	
		c	PC	3.31		3.03	4.42	13.40	0.990	13.27	0.006	"	Gusev Heavy Crplains
Meridiani	2	a	PC	2.9		4.89	9.45	24.38	0.791	19.29	0.037	Albedo variations, not slopes	
		b	PC	2.9		1.25	1.82	4.94	0.946	4.68	<0.001	Bland area, typical	
		c	PC	2.9		2.21	3.38	9.46	0.933	8.83	<0.001	Exposed rougher area	
Meridiani	4	a	ST	10	1.63	1.61	2.25	7.35	1.048	7.70	<0.001	Plains and subdued crater	
		b	ST	10	1.63	1.44	1.92	5.62	1.048	5.89	<0.001	Plains only	Meridiani Plains
		c	ST	10	1.63	2.52	3.76	10.81	1.061	11.47	0.003	Subdued crater only	Meridiani Crater
Meridiani	5	a	ST	10	1.13	1.26	2.27	5.19	1.050	5.44	<0.001	Plains and subdued crater	

^aPC = photocliometry, ST = stereo. ^bAll slopes in degrees. ^cError in bidirectional slopes from stereo based on tests described in text. ^dBdir = bidirectional slope in sample direction. ^eAdir = adirectional slope (gradient). ^fFactor to correct slope from indicated baseline to 5 m, based on Hurst exponent; see text. ^gIncludes indication why results in gray are considered unreliable or not representative of site.

Table 4. Photoclinometric Analysis of Simulated Images with Uniform Albedo

Nominal RMS Slope ^{a,b}	Hurst Exponent <i>H</i>	Filter ^c	Sun Azimuth ^d	Exact RMS Height	RMS Height Error ^e	RMS Height Error (Destriped) ^f	Exact RMS Slope ^g	PC RMS Slope	% Error in PC Slope
1	0.2		0	0.2518	0.6399	0.0182	0.9999	0.9971	-0.28
1	0.2		22.5	0.2518	0.6078	0.0469	0.9999	1.0132	1.33
1	0.5		0	0.8772	0.7763	0.0174	1.0000	0.9976	-0.24
1	0.5		22.5	0.8772	0.7411	0.0411	1.0000	1.0100	1.00
1	0.8		0	3.0545	2.2273	0.0214	1.0000	0.9976	-0.24
1	0.8		22.5	3.0545	2.1370	0.0415	1.0000	1.0031	0.31
1	0.8	Lowpass	0	3.0510	2.1977	0.0160	0.9006	0.8986	-0.22
1	0.8	Lowpass	22.5	3.0510	2.1350	0.0228	0.9006	0.9064	0.64
1	0.8		0	3.0545	2.2273	0.0214	1.0000	0.9976	-0.24
1	0.8		22.5	3.0545	2.1370	0.0415	1.0000	1.0031	0.31
1	0.8	Highpass	0	0.2717	0.3448	0.0141	0.5203	0.5196	-0.13
1	0.8	Highpass	22.5	0.2717	0.3320	0.0301	0.5203	0.5143	-1.15
1	0.8		0	3.0545	2.2273	0.0214	1.0000	0.9976	-0.24
1	0.8		22.5	3.0545	2.1370	0.0415	1.0000	1.0031	0.31
10	0.8		0	30.5451	40.9136	1.5424	9.9917	9.4691	-5.23
10	0.8		22.5	30.5451	37.1268	2.2806	9.9917	9.2364	-7.56

All simulated images 1024x1024 pixels at 3 m/pixel. Nominal case (1° slope, $H=0.8$, unfiltered) is repeated for clarity. ^aSlopes in degrees, bidirectional in sample direction between adjacent pixel centers. ^bDEMs are scaled to have specified RMS bidirectional slope before filtering. ^cLowpass, highpass filtered DEMs omit roughness elements smaller, larger than 16 pixels respectively. ^dAzimuth in degrees from direction in which slopes are measured; incidence angle 45° in all cases. ^eDifference between photoclinometric estimate and exact DEM. ^fDifference after subtracting means within profiles aligned with sun. ^gAs measured.

Table 5. Photoclinometric Analysis of Simulated Images with Variable Albedo

Sun Azimuth	RMS Slope Constant Albedo	RMS Slope Variable Albedo	RMS Slope Variable Albedo (Destriped)
0	0.9976	1.1212	1.1043
22.5	1.0031	1.3585	0.9753
45	0.9959	2.0827	0.9520
67.5	0.9850	2.0799	0.9900
90	0.9471	2.5250	1.1200

All simulated images 1024x1024 pixels at 3 m/pixel, nominal slope 1°, $H=0.8$.

10. Figures

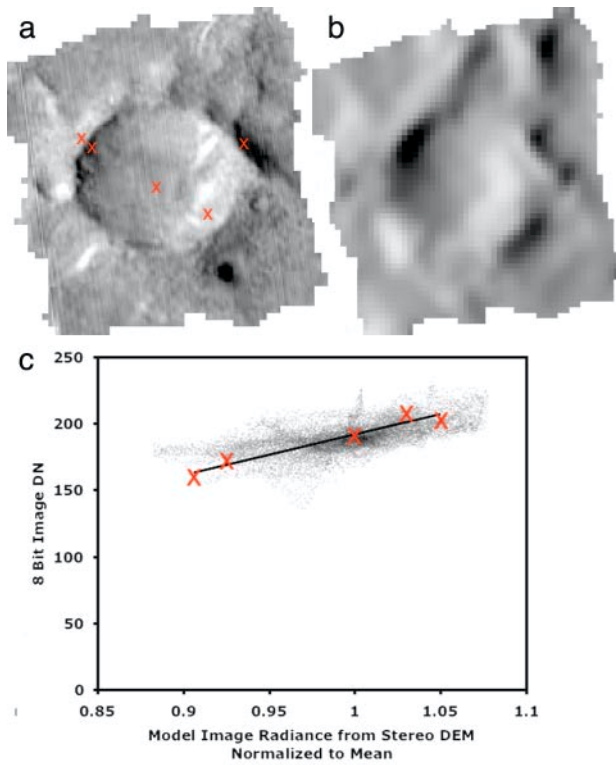


Figure 1

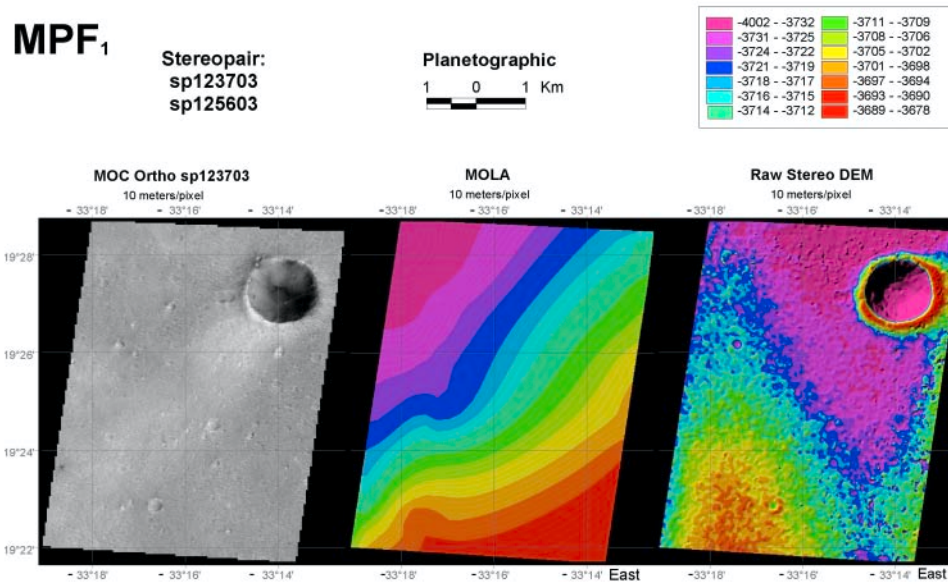


Figure 2

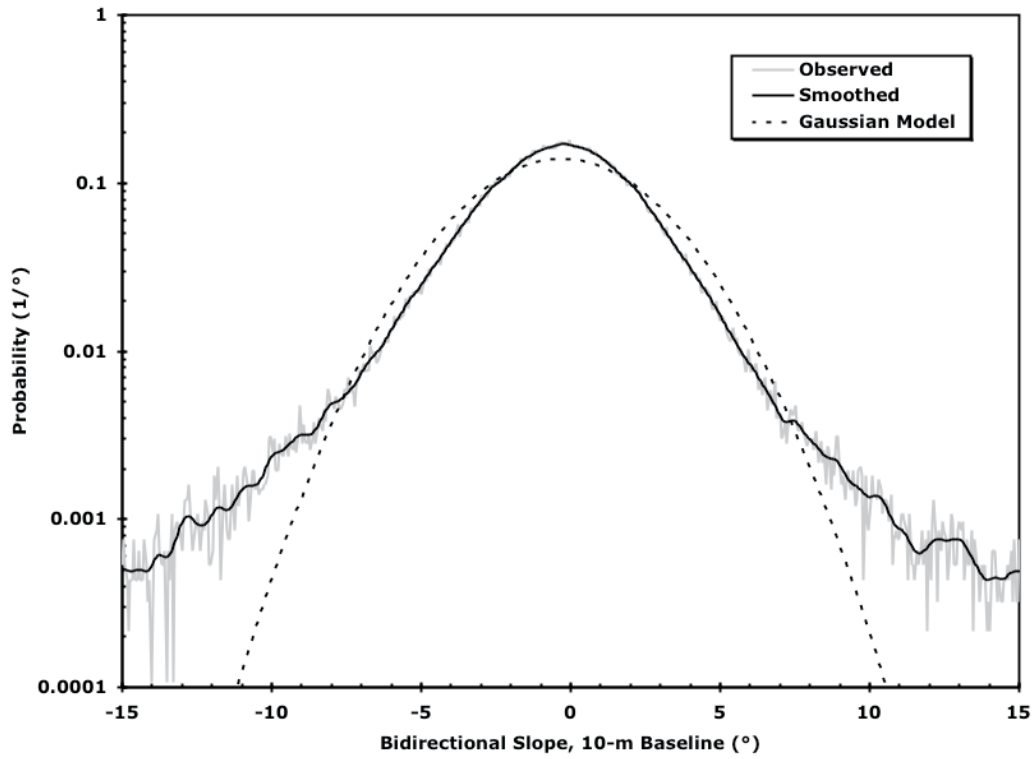


Figure 3

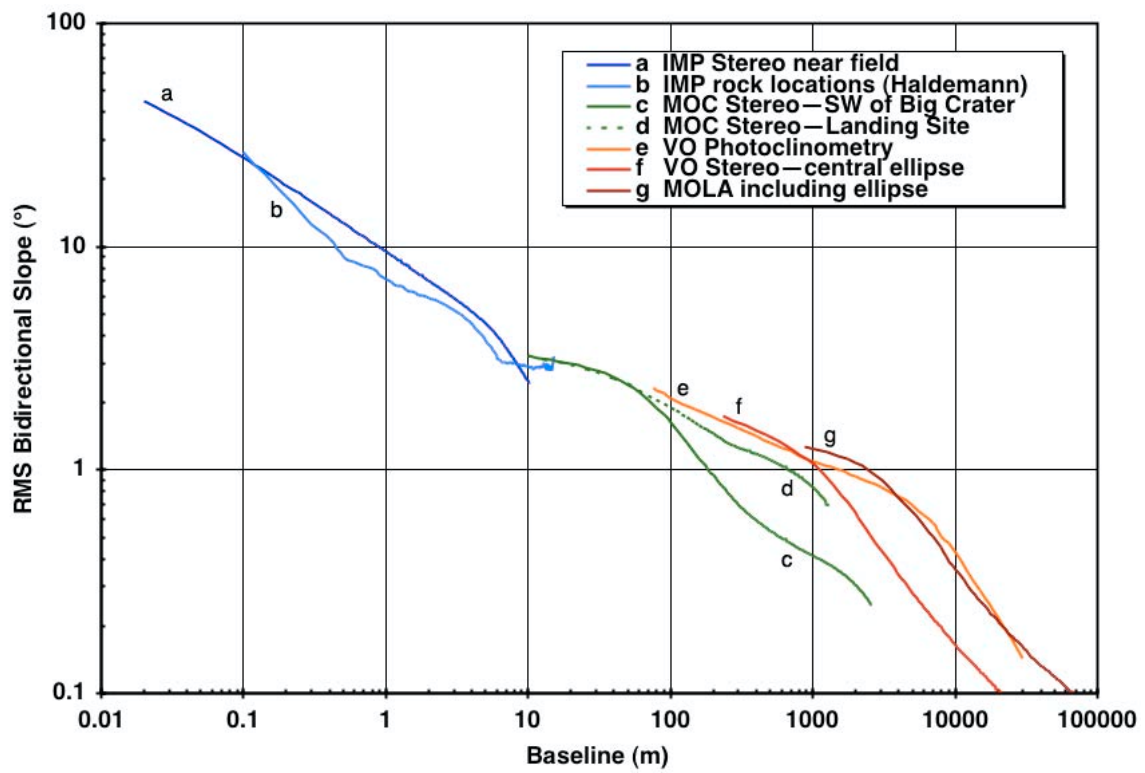


Figure 4.

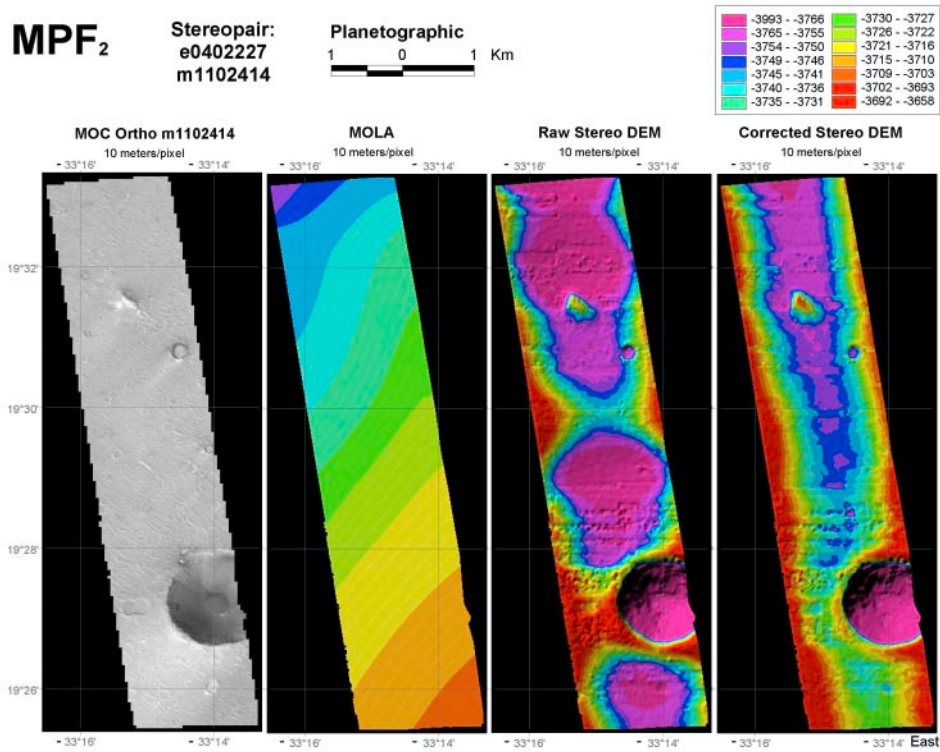


Figure 5

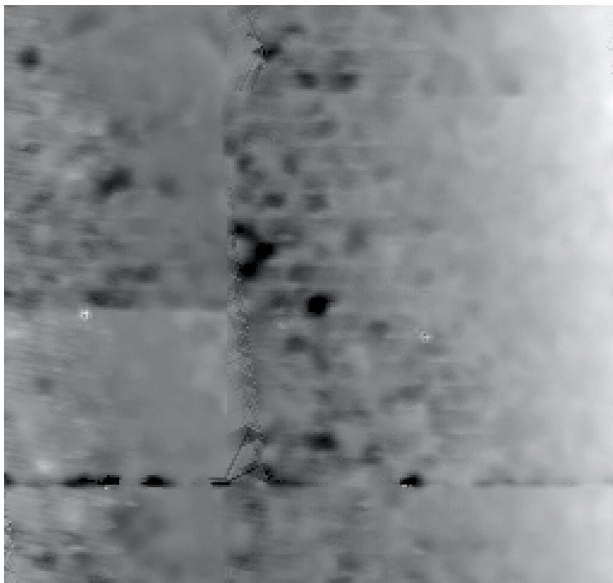


Figure 6

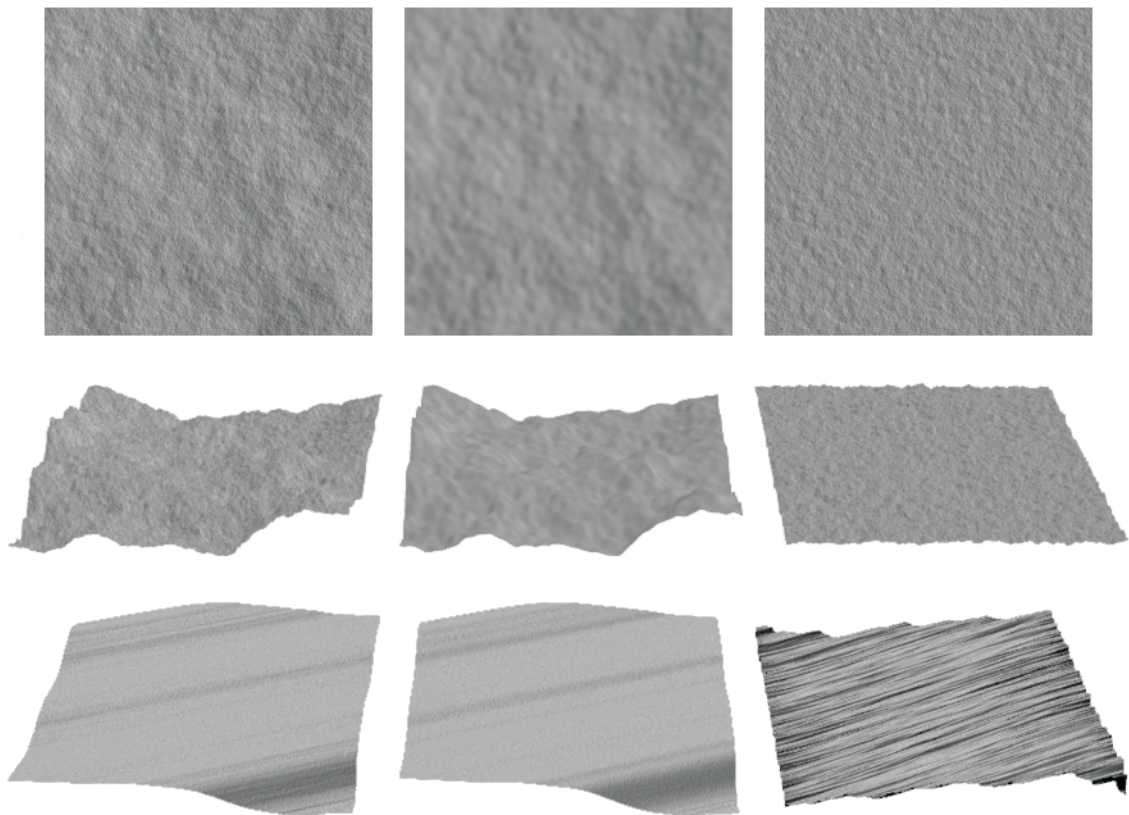


Figure 7

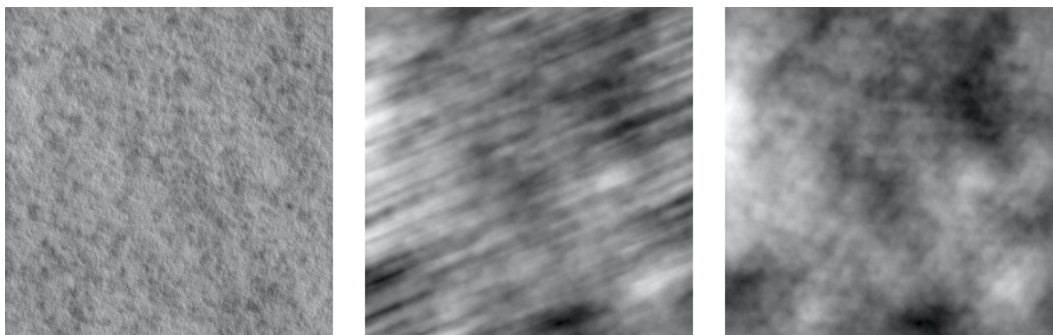


Figure 8

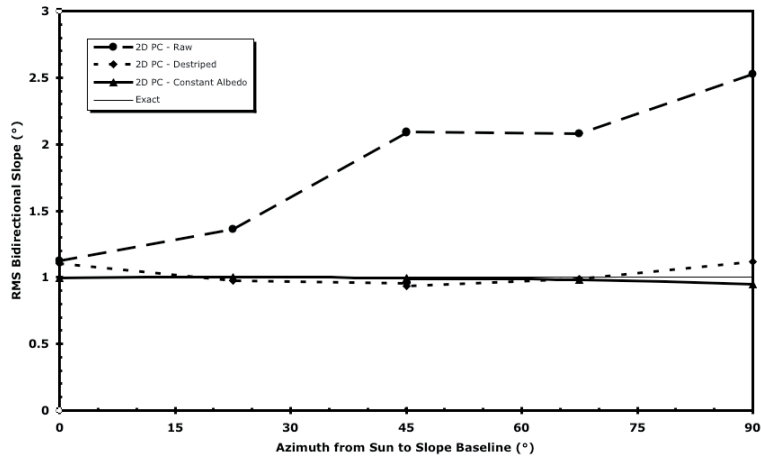


Figure 9

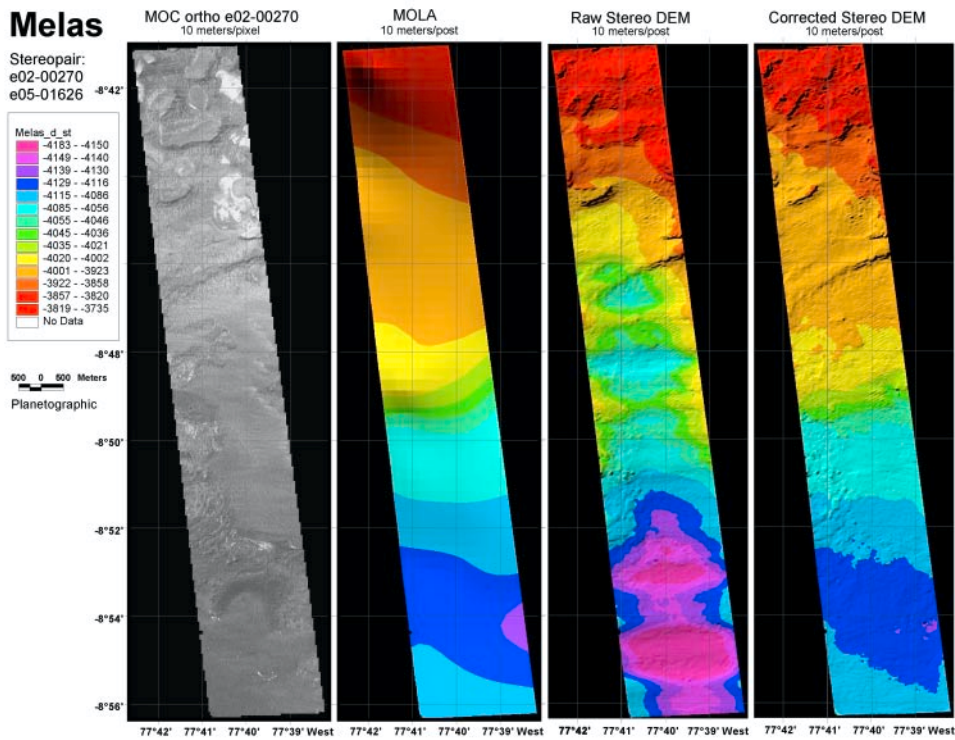


Figure 10

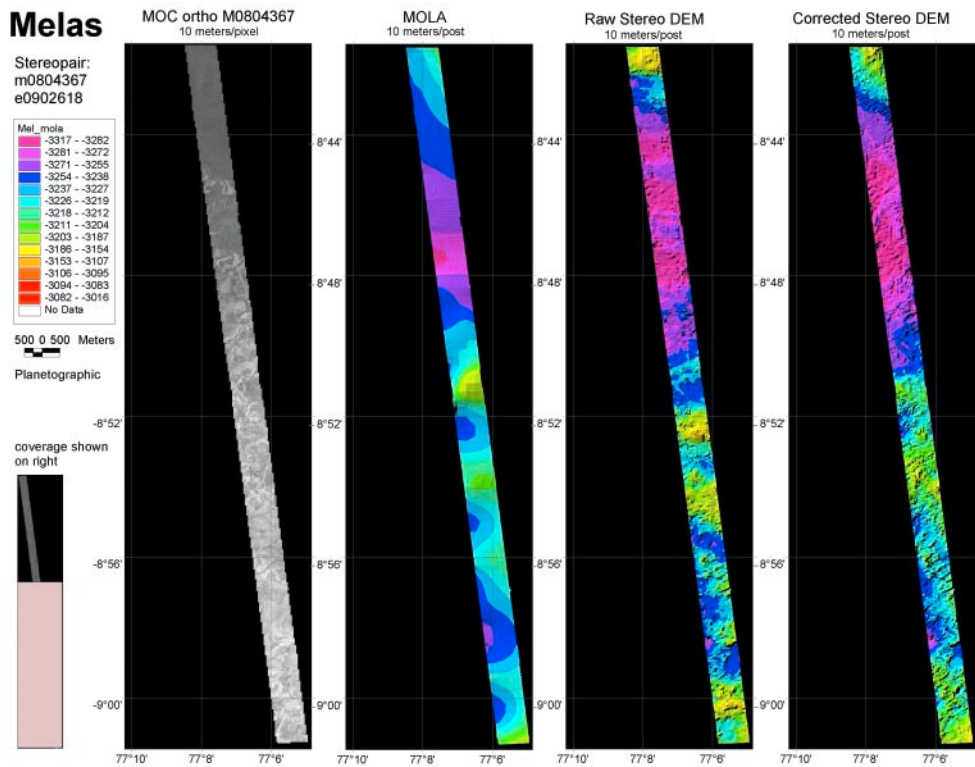


Figure 11

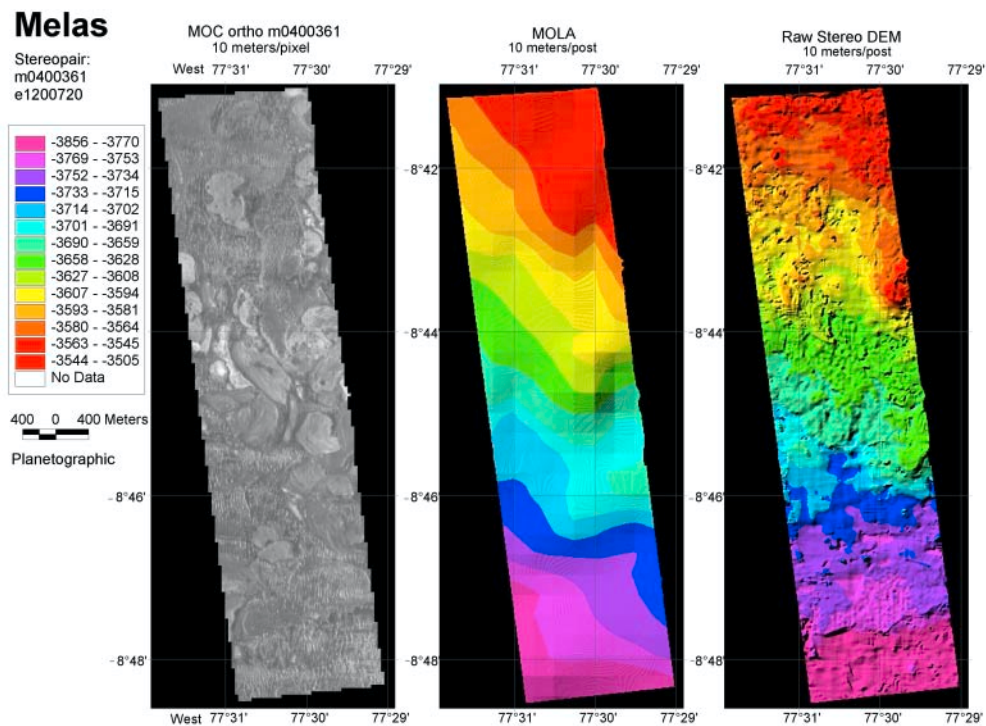


Figure 12

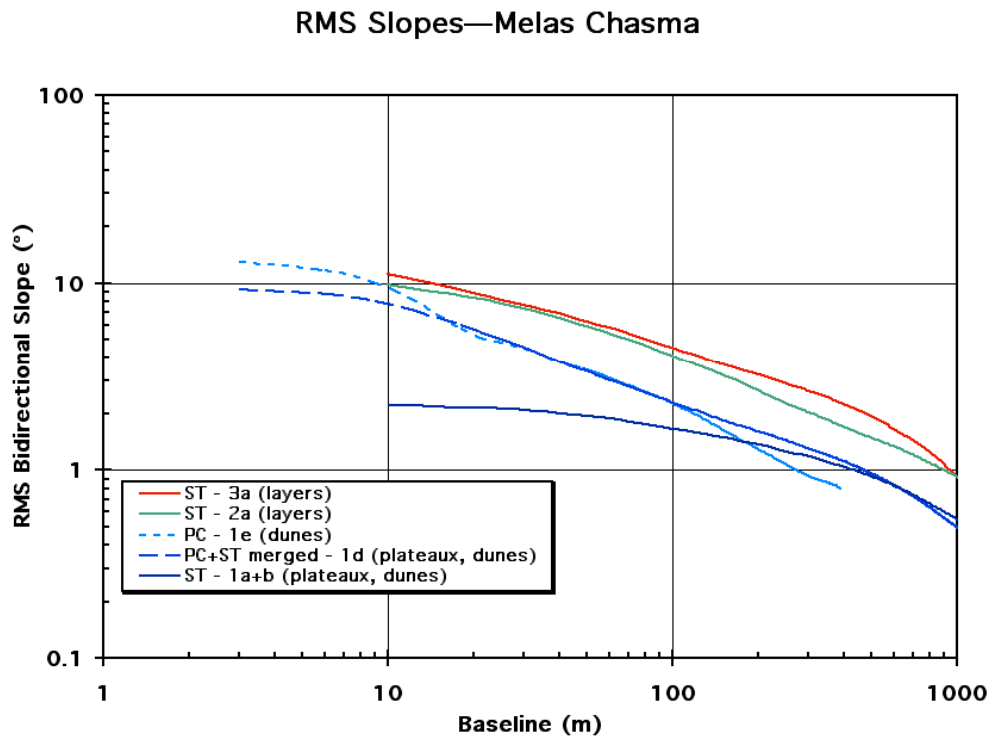


Figure 13

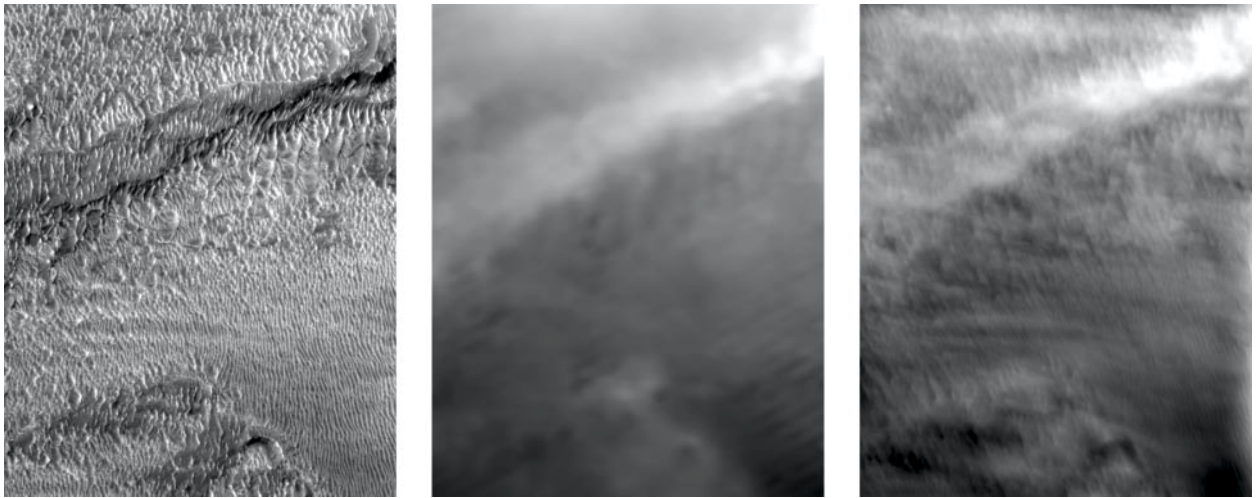


Figure 14

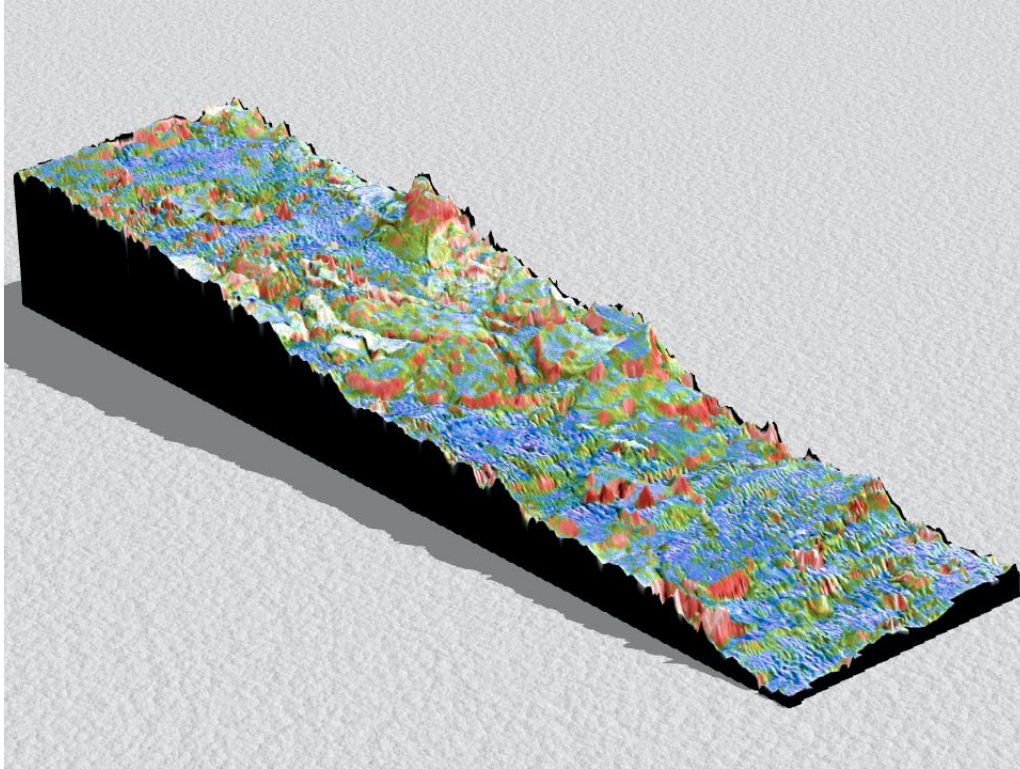


Figure 15

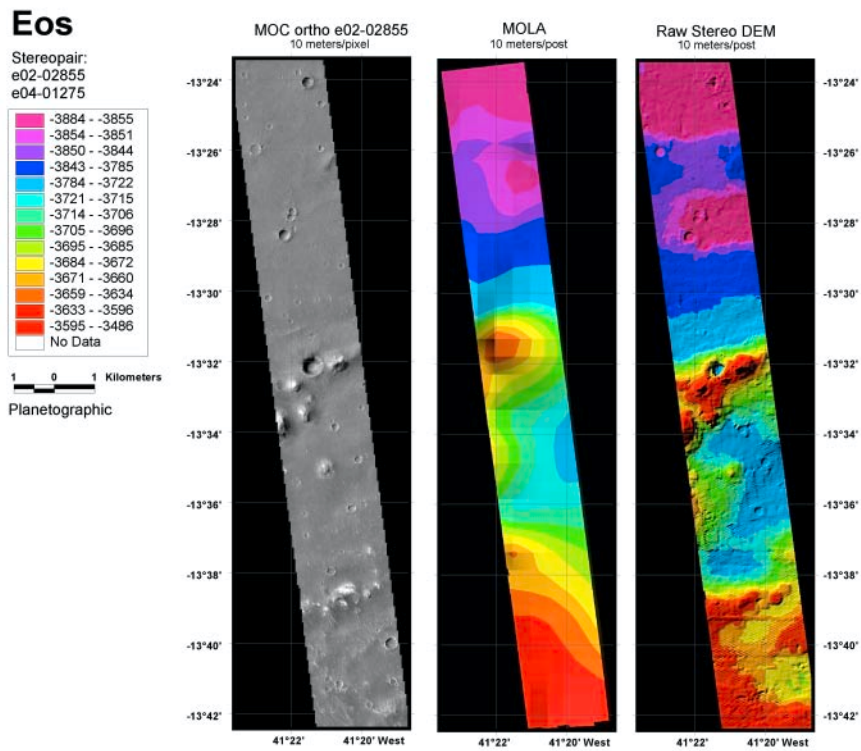


Figure 16

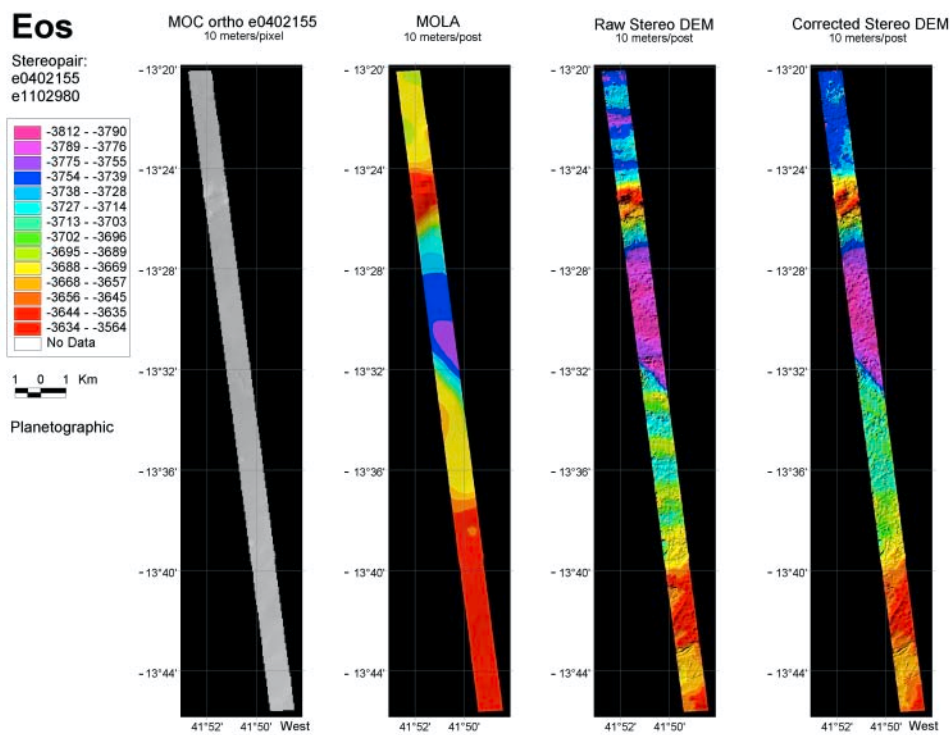


Figure 17

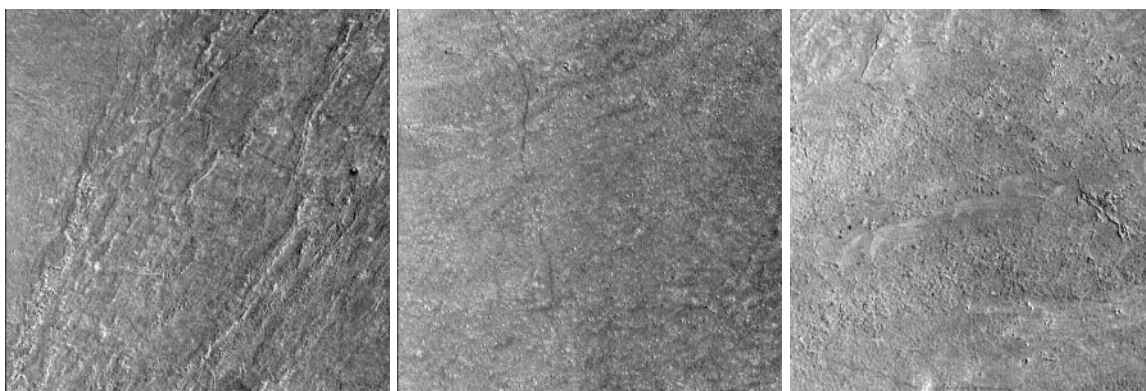
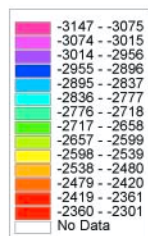


Figure 18

Athabasca

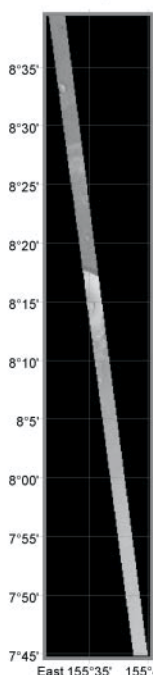
Stereopair:
m07-05928
e10-02604



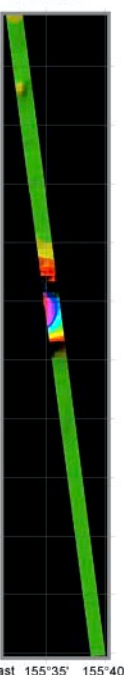
2 0 2 Kilometers

Planetographic

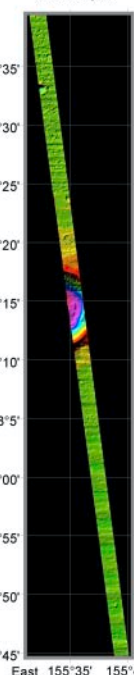
MOC ortho m07-05928
20 meters/pixel



MOLA
20 meters/post



Raw Stereo DEM
20 meters/post



Corrected Stereo DEM
20 meters/post

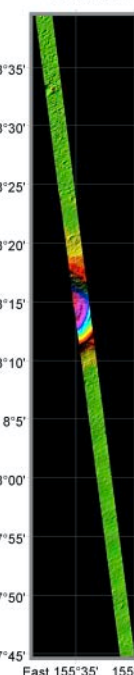
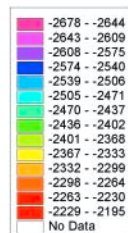


Figure 19

Athabasca

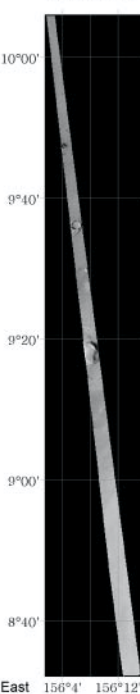
Stereopair:
m0700614
e0500197



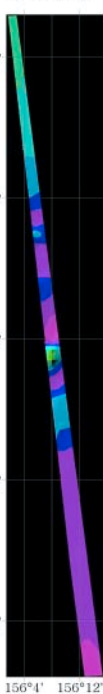
4 0 4 Km

Planetographic

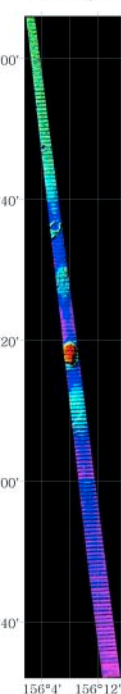
MOC ortho M0700614
20 meters/pixel



MOLA
20 meters/post



Raw Stereo DEM
20 meters/post



Corrected Stereo DEM
20 meters/post

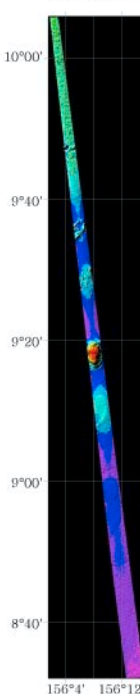


Figure 20

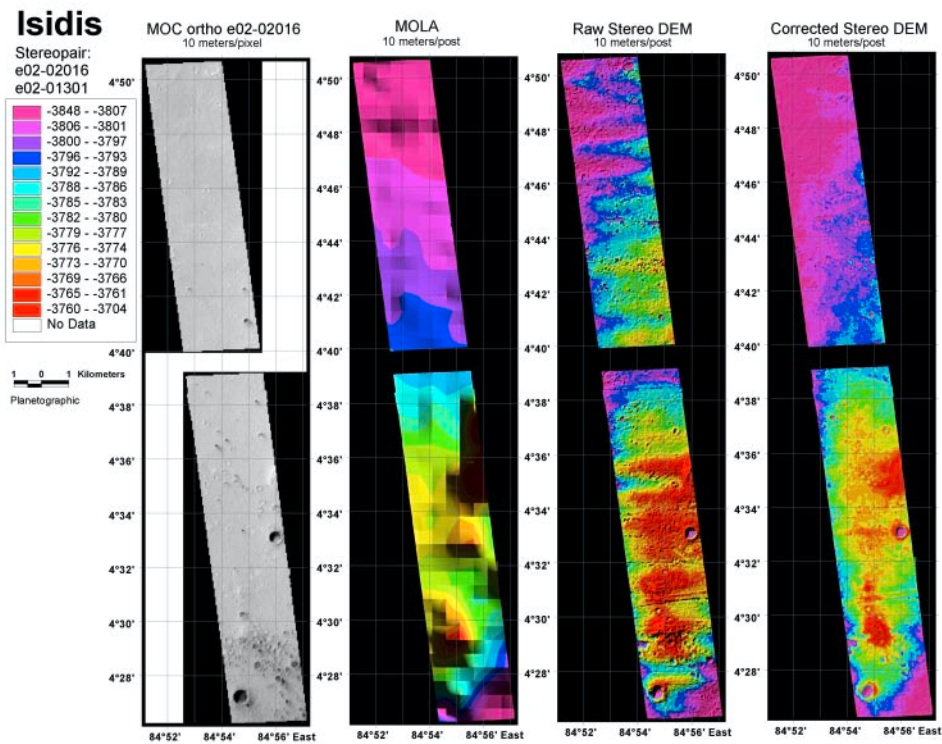


Figure 21

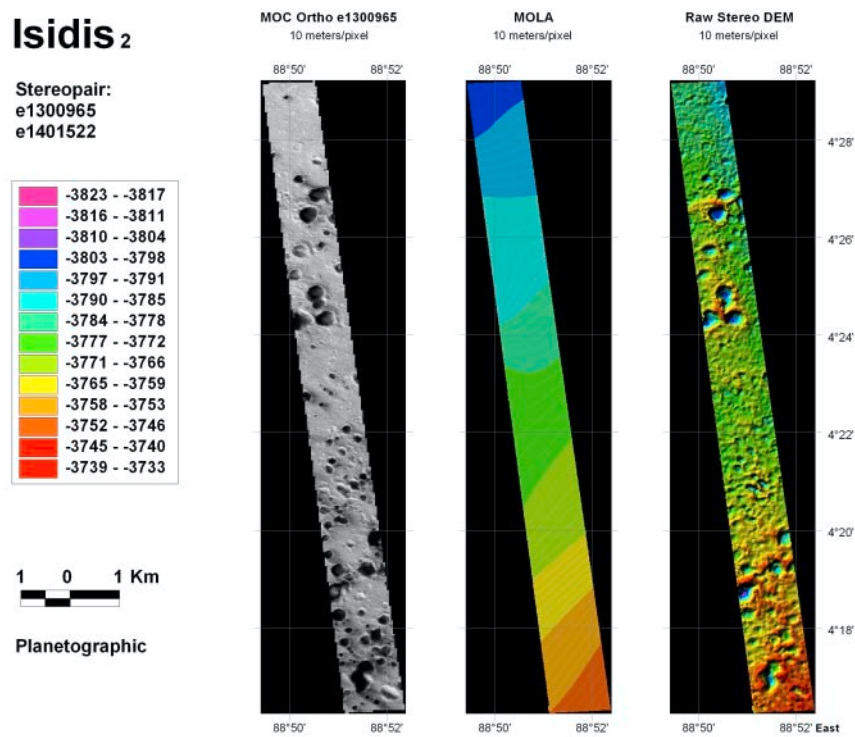


Figure 22

Elysium 1

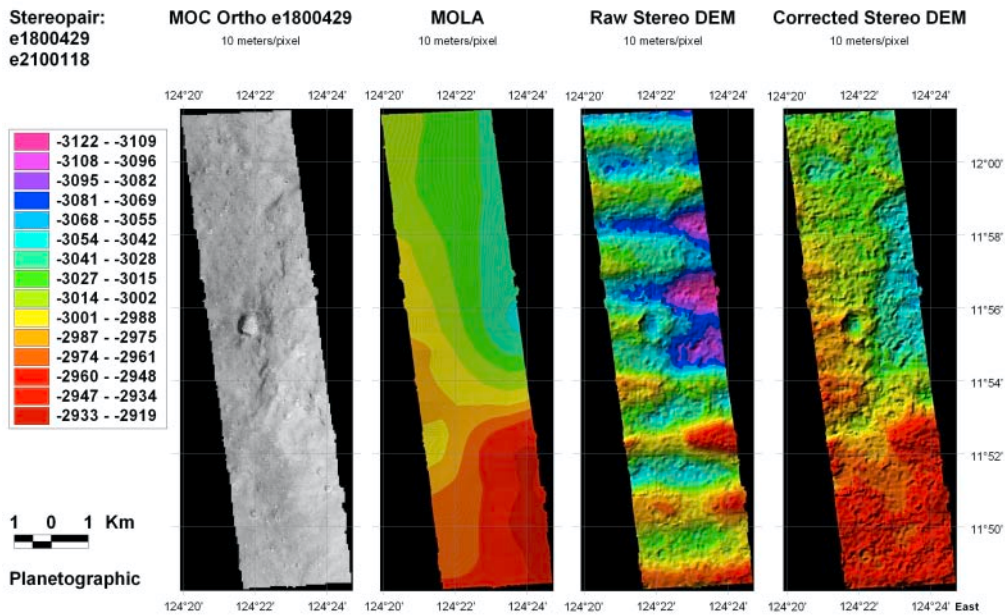


Figure 23

Elysium 2

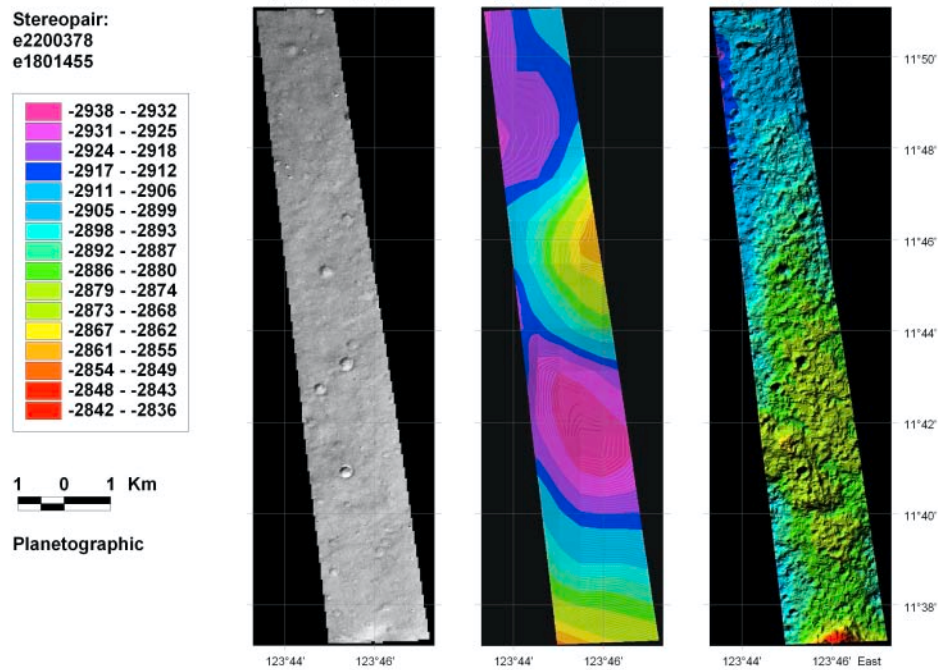


Figure 24

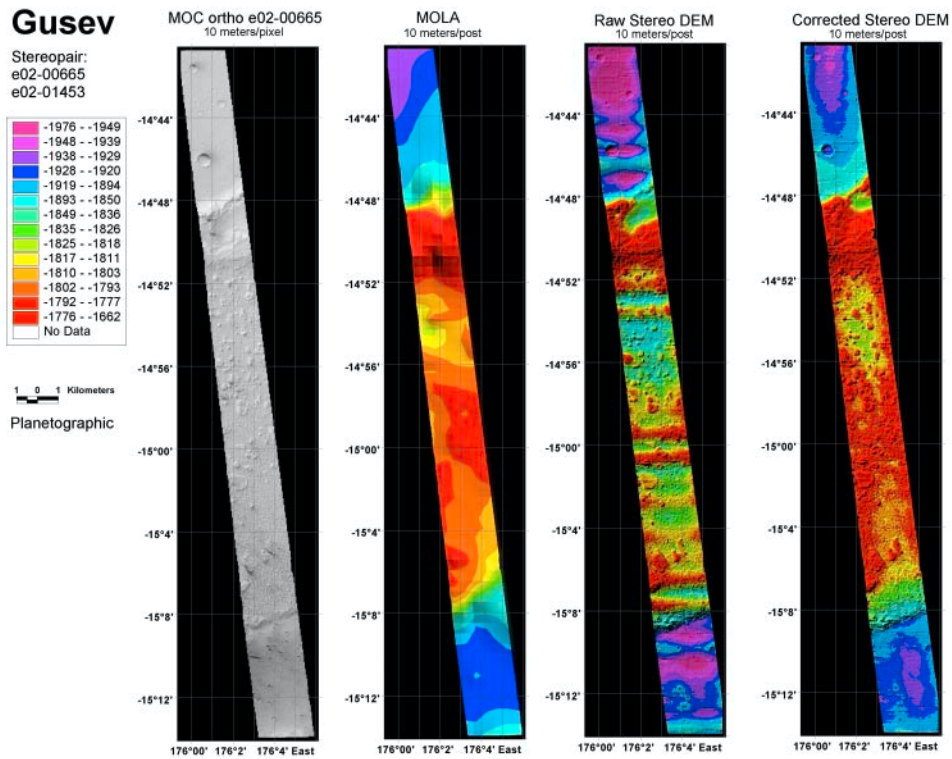


Figure 25

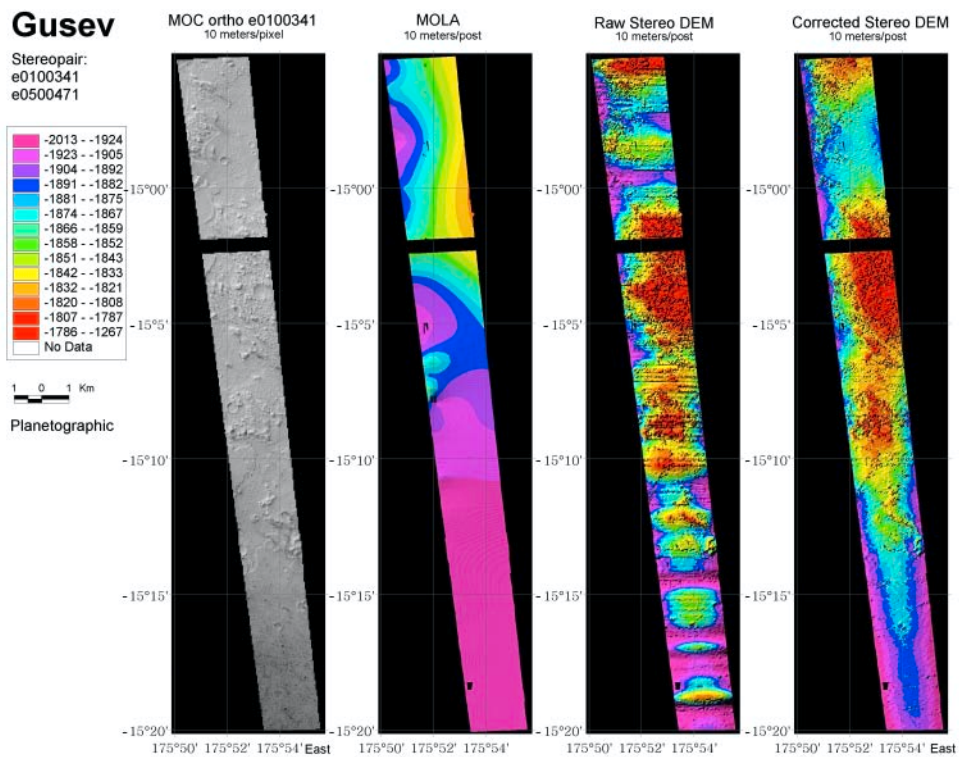


Figure 26

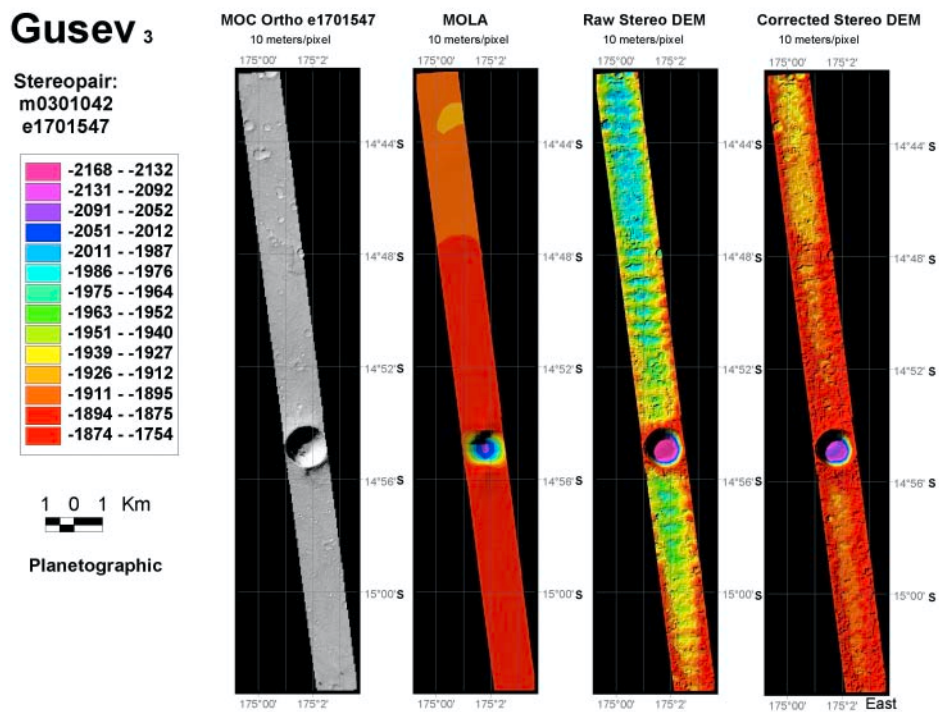


Figure 27

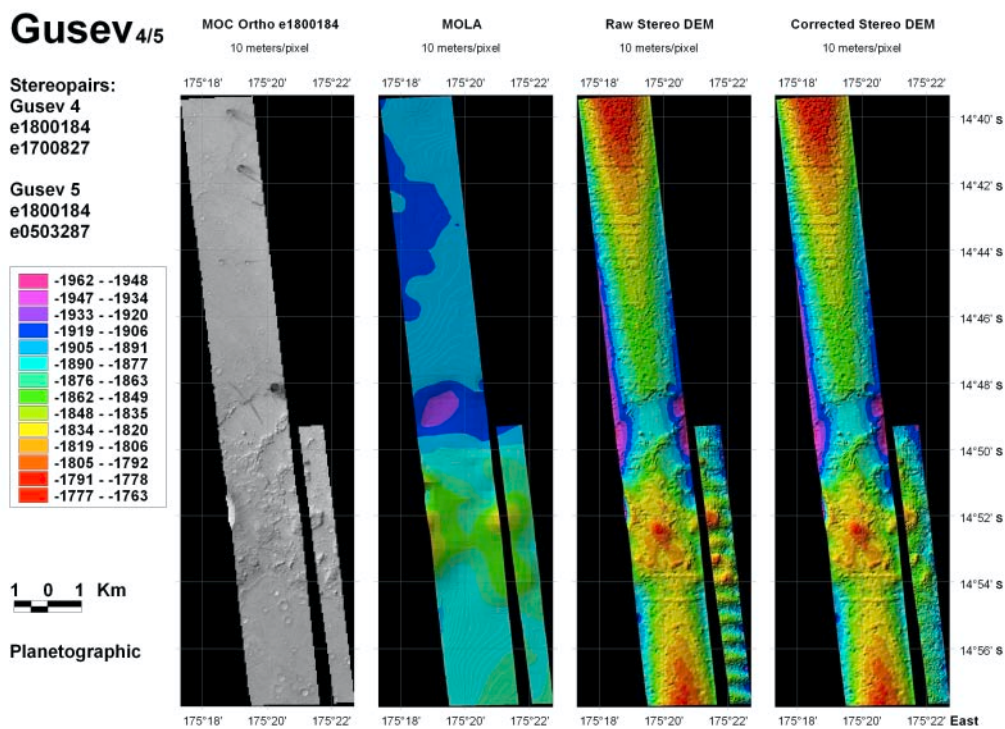
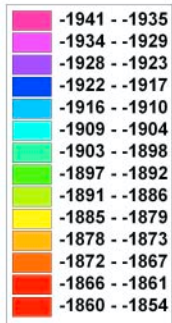


Figure 28

Gusev₆

Stereopair:
e1900218
e2100256



1 0 1 Km

Planetographic

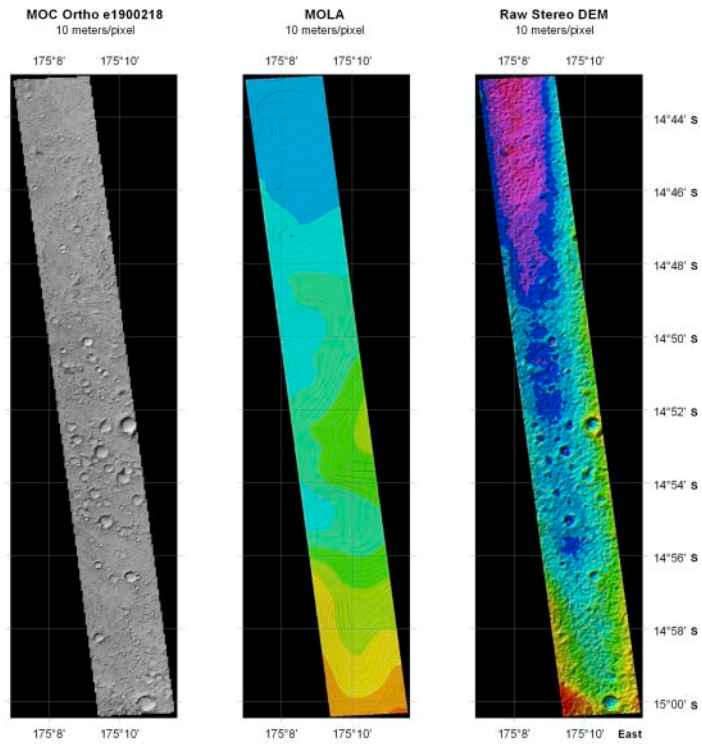


Figure 29

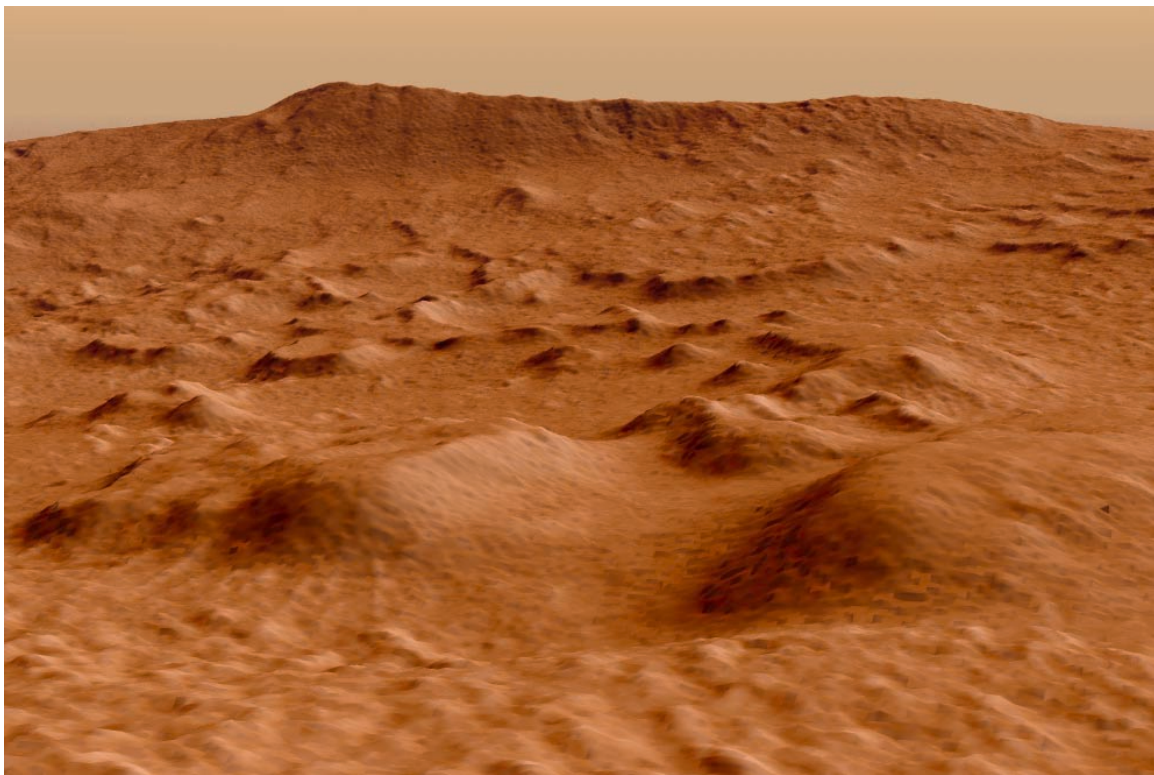


Figure 30

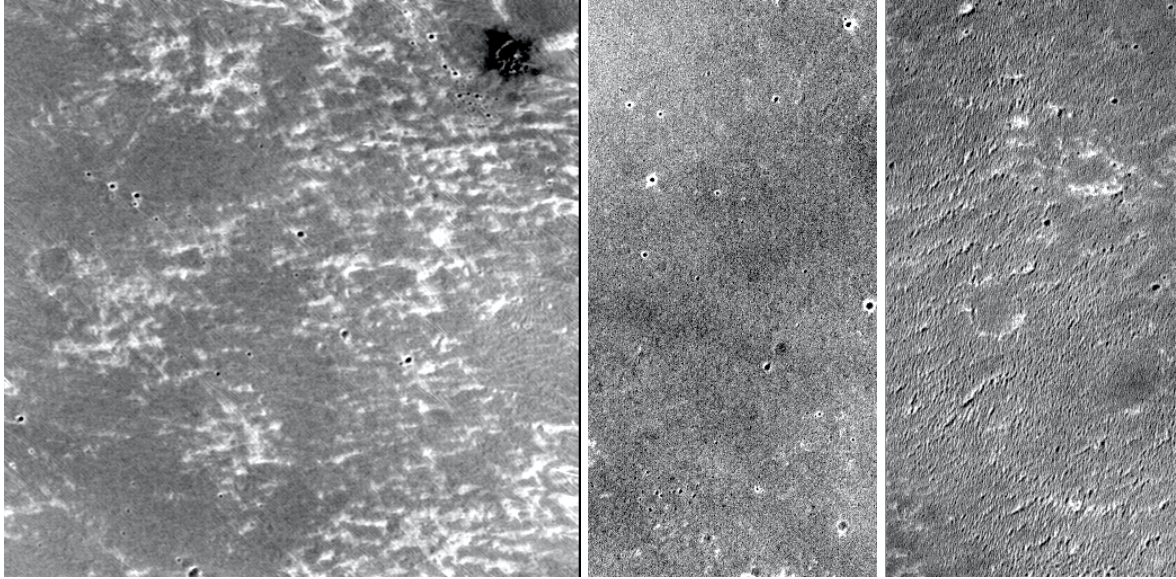


Figure 31

Hematite₄

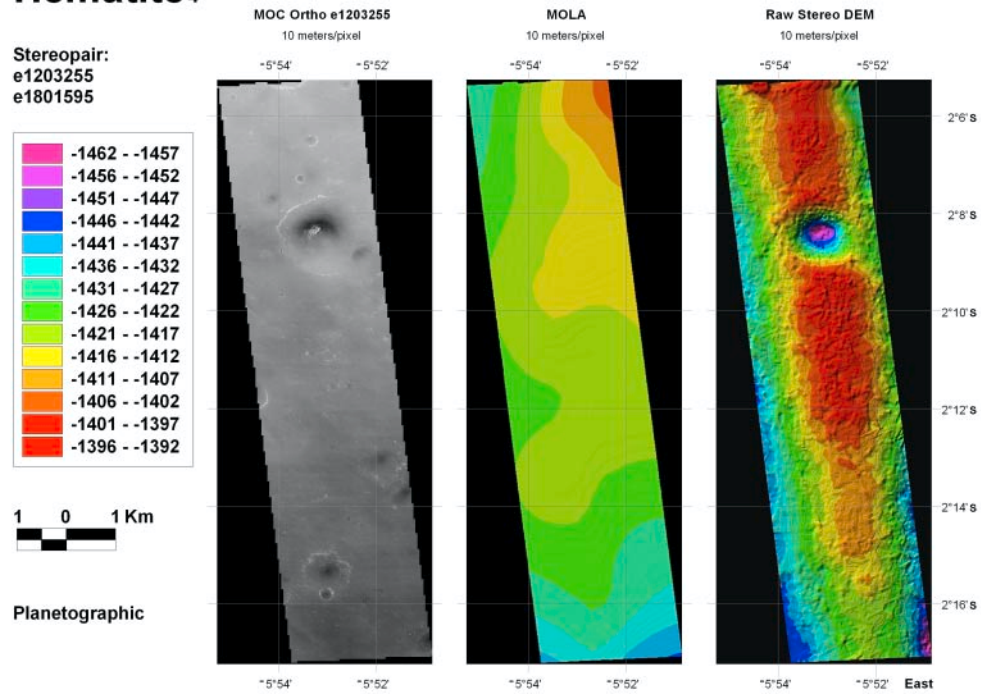
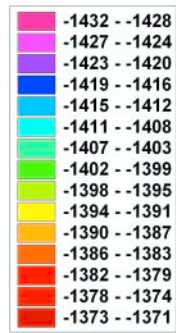


Figure 32

Hematite₅

Stereopair:
e1500023
e2101653



1 0 1 Km

Planetographic

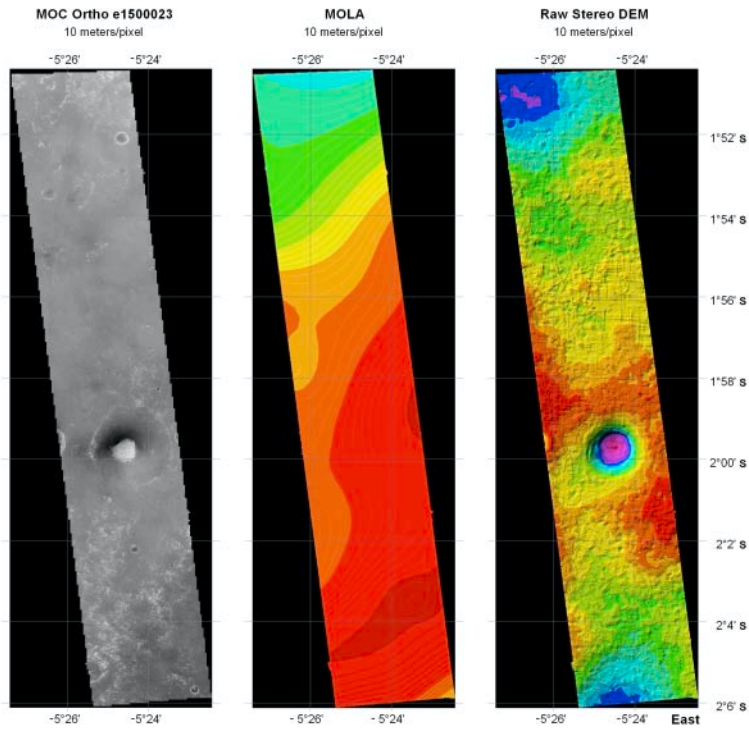


Figure 33

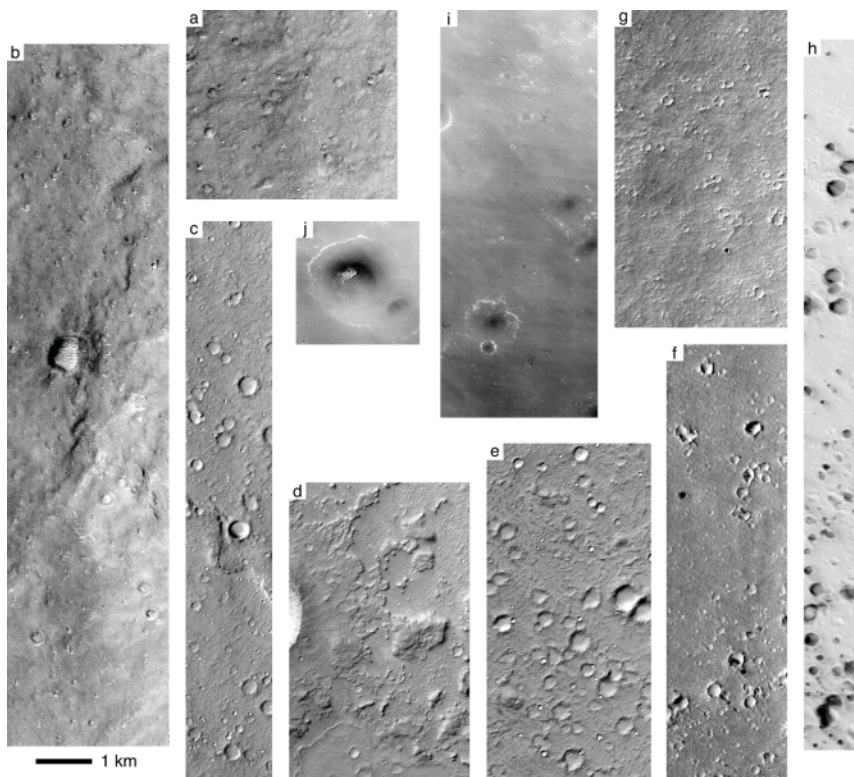


Figure 34

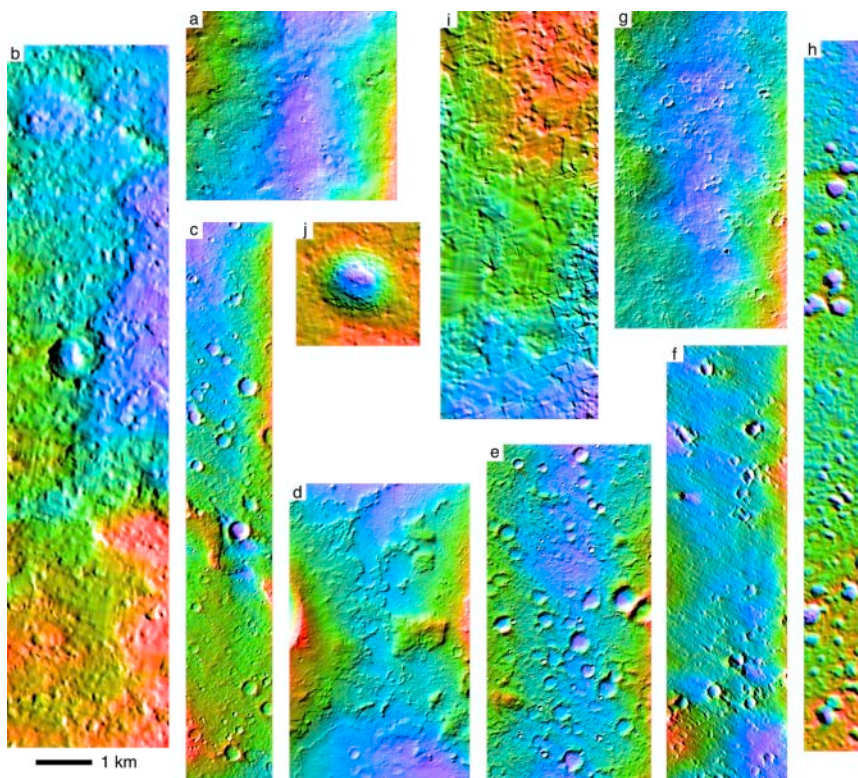


Figure 35

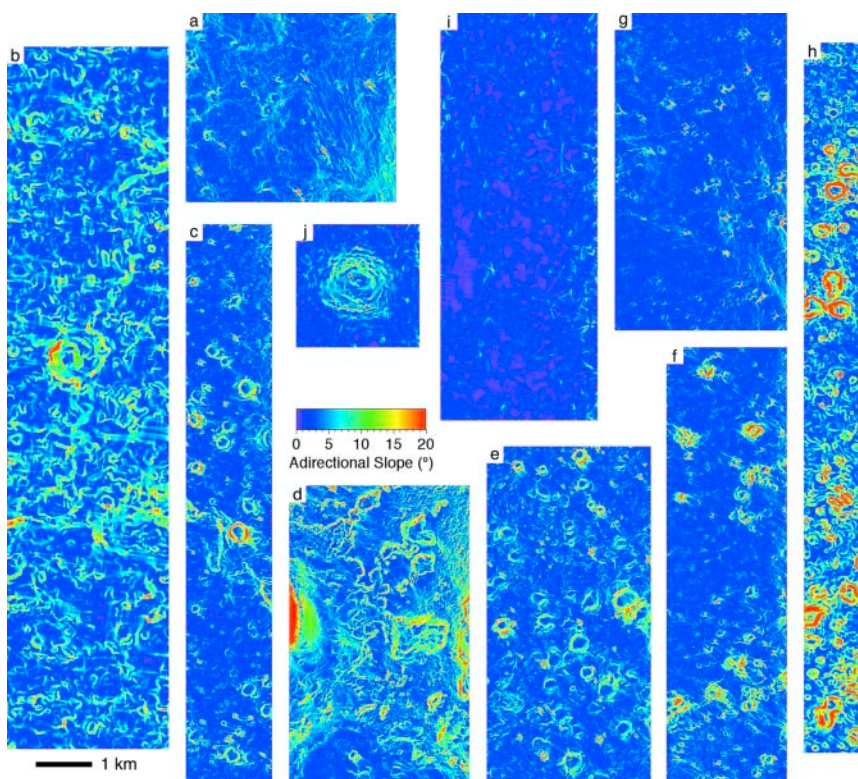


Figure 36

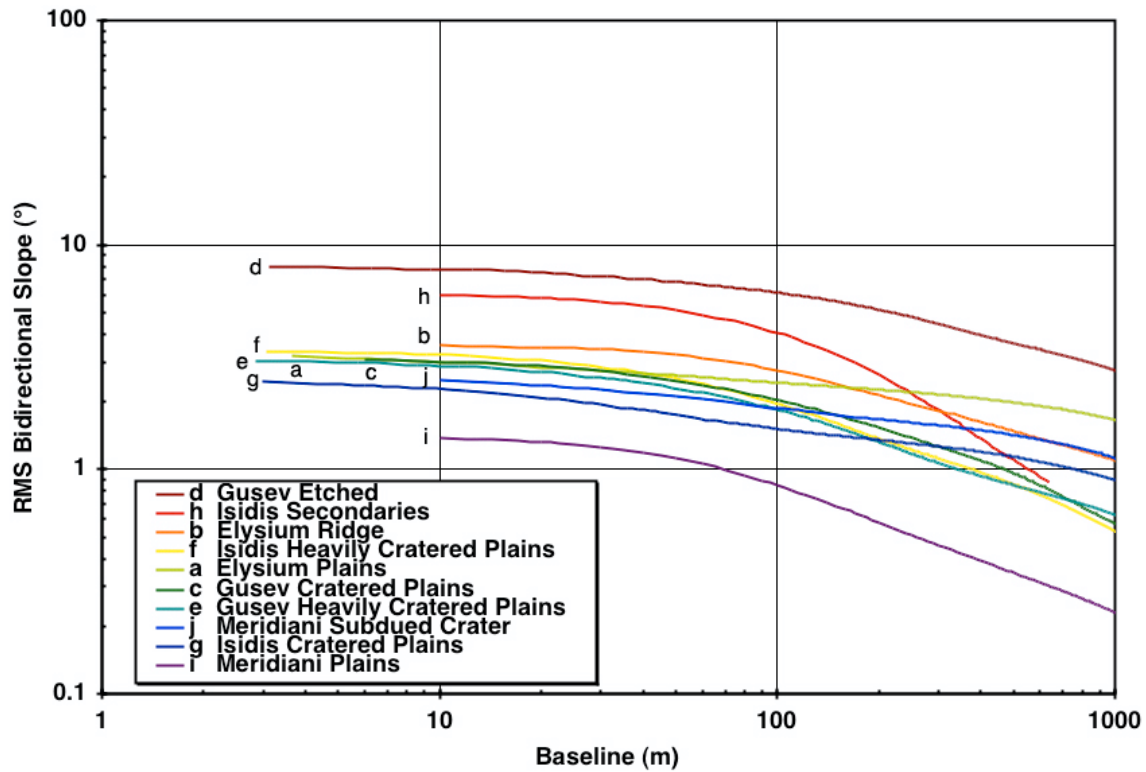


Figure 37

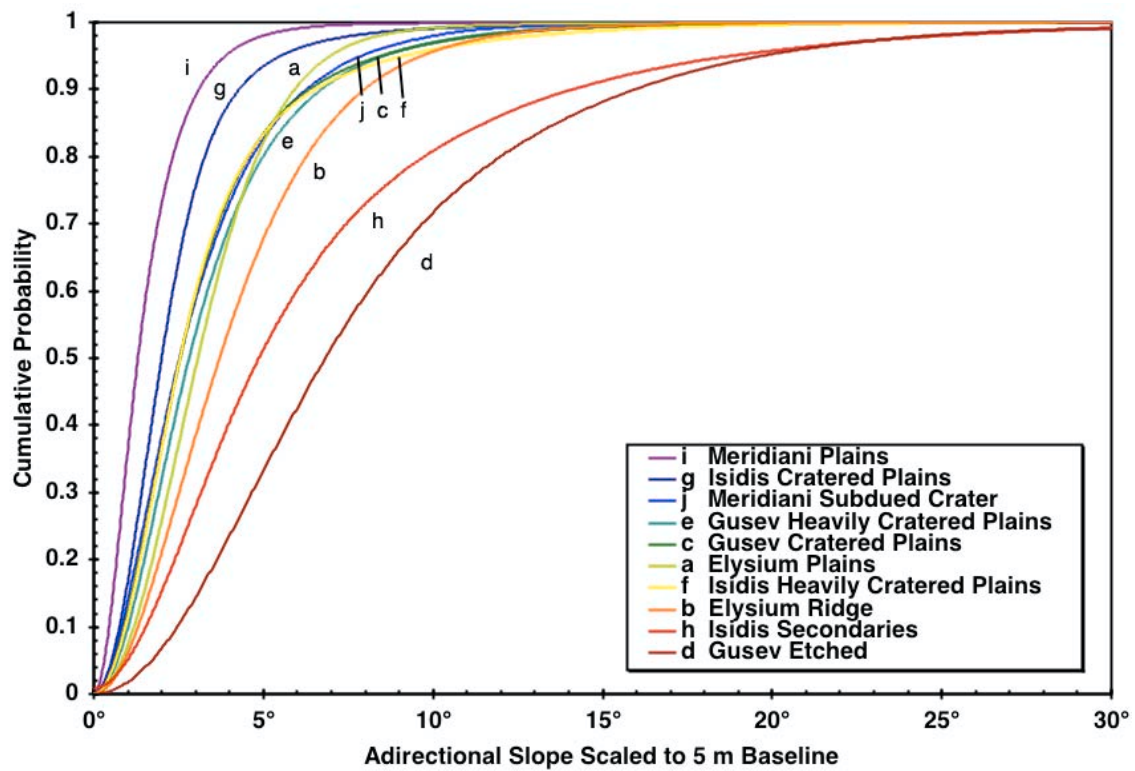


Figure 38